Emergent effects of synaptic connectivity on the dynamics of global and local slow waves in a large-scale thalamocortical network model of the human brain

Brianna M Marsh[1,2†], **M. Gabriela Navas-Zuloaga**[1†], **Burke Q Rosen**[2], **Yury Sokolov**[1], **Jean Erik Delanois**[1,3], **Oscar C González**[1], **Giri P. Krishnan**[1], **Eric Halgren**[2,4], **Maxim Bazhenov**[1,2]

***For correspondence:** mbazhenov@ucsd.edu (MB)

[†]These authors contributed equally to this work

[1]Department of Medicine, University of California, San Diego ; [2]Neuroscience Graduate Program, University of California, San Diego ; [3]Department of Computer Science and Engineering, University of California, San Diego ; [4]Departments of Radiology and Neuroscience, University of California, San Diego

Abstract Slow-wave sleep (SWS), characterized by slow oscillations (SO, <1Hz) of alternating active and silent states in the thalamocortical network, is a primary brain state during Non-Rapid Eye Movement (NREM) sleep. In the last two decades, the traditional view of SWS as a global and uniform whole-brain state has been challenged by a growing body of evidence indicating that sleep oscillations can be local and can coexist with wake-like activity. However, the understanding of how global and local SO emerges from micro-scale neuron dynamics and network connectivity remains unclear. We developed a multi-scale, biophysically realistic human whole-brain thalamocortical network model capable of transitioning between the awake state and slow-wave sleep, and we investigated the role of connectivity in the spatio-temporal dynamics of sleep SO. We found that the overall strength and a relative balance between long and short-range synaptic connections determined the network state. Models with relatively weaker long-range connectivity resulted in mixed states of global and local slow waves. Increase of synaptic strength led to more synchronized global SO. These results were compared to human data to validate probable models of biophysically realistic slow waves. The model producing mixed states provided the best match to the spatial coherence profiles obtained in the human subjects. These findings shed light on how the spatio-temporal properties of SO emerge from local and global cortical connectivity and provide a framework for further exploring the mechanisms and functions of SWS in health and disease.

Introduction

Internal states of the brain rapidly and profoundly influence sensation, cognition, emotion, and action (***Lee and Dan, 2012***; ***Pfaff et al., 2008***; ***Steriade and McCarley, 2013***). Dramatic change of internal brain state occurs at the transition between wakefulness and sleep (***Campbell and Tobler, 1984***; ***Leung and Mourrain, 2018***; ***Steriade and McCarley, 2013***). The main electrophysiological hall-

marks of slow wave sleep (SWS) and rapid eye movement (REM) sleep are shared across mammals. During the SWS, the brain dynamics is dominated by oscillations between an active Up and a silent Down state, the activity called slow oscillation (SO, <1Hz) (***Steriade et al., 1993a***,b). Alterations of these sleep dynamics have significant consequences for brain function and are at the core of many neuropsychiatric disorders (***Winkelman and Lecea, 2020***).

Until recently, sleep/wake transitions or transitions between different stages of sleep were thought to occur uniformly throughout the cortex. Recent evidence in rodents, primates and humans points to the existence of electrographic events resembling local sleep during behavioral wakefulness (***Vyazovskiy et al., 2011***; ***Hung et al., 2013***; ***Quercia et al., 2018***; ***Engel et al., 2016***; ***van Kempen et al., 2021***). During wakefulness, local groups of cortical neurons tend to fall silent for brief periods, as they do during SWS. Similarly, during behavioral sleep, transient local wake-like activity can intrude SWS (***Nobili et al., 2011***; ***Peter-Derex et al., 2015***). SWS and REM sleep can also coexist in different cortical areas (***Soltani et al., 2019***; ***Funk et al., 2016***; ***Bernardi et al., 2018***). Homeostatic sleep pressure can affect cortical activity locally (***Siclari and Tononi, 2017***). Spindles and slow waves, may increase locally after learning (***Eschenko et al., 2006***; ***Pugin et al., 2015***), suggesting experience dependent regulation. Together these results suggest an intriguing idea that local slow-waves may have a functional significance enabling brain to process and learn in a parallel way. However, the underlying mechanisms of local vs global slow-wave dynamics as well as factors controlling transitions between them are unknown.

We previously developed computer models of sleep SO (***Timofeev et al., 2000***; ***Bazhenov et al., 2002***), including transitions between awake and sleep states (***Krishnan et al., 2016***). However, the highly detailed and computationally intensive nature of these models have prevented up-scaling to investigate slow wave dynamics at the whole-brain scale. Recently, several whole-brain models of slow-wave sleep incorporating biologically grounded connectivity from probabilistic diffusion MRI tractography and providing a good fit to human sleep recordings were proposed (***Cakan et al., 2022***; ***Goldman et al., 2023***). These models investigated the role of long-range connections in SO brain-wide propagation. However, the mean-field neural-mass representation of cortical regions in these models provides only limited insights on how local (within a few milimeters) and long-range connectivity and activity interact to affect initiation and propagation of sleep slow waves.

To bridge this gap between micro and macro-scale mechanisms, we have developed a multi-scale, whole-brain, thalamocortical network model with biologically grounded cortical connectivity that exhibits the essential activity states of wake and slow wave sleep. The model consists of 10,242 cortical columns per hemishpere, each containing spiking pyramidal (PY) and inhibitory (IN) neurons arrayed in 6 layers, and 642 thalamic cells of each of four types (thalamo-cortical (TC) and reticular (RE), belonging to either core or matrix). To investigate the role of connectivity in emerging SO, we systematically modified the density, range, and relative strength of cortical connections, as well as distance-dependent synaptic delays. The model dynamics were compared to the spatial coherence profiles obtained from human subjects. Our study predicted that a characteristic balance of long and short-range connectivity is necessary to match the data and enable the emergence of complex mixed states of local and global slow oscillations (SOs) (***Nir et al., 2011***; ***Bernardi et al., 2018***; ***Vyazovskiy et al., 2009***). Furthermore, changes in synaptic weights, which likely occur during sleep (***Timofeev and Chauvette, 2017***), may enable transitions between global synchronized and local SOs.

Results

Connectivity

We start with a brief overview of the model (***Figure 1***, see Methods for details). The model includes 10,242 cortical columns positioned uniformly across the surface of one hemisphere, corresponding to the vertices in the ico5 cortical reconstruction reported in (***Rosen et al., 2019***). The medial wall includes 870 of these vertices, so all analyses for this one-hemisphere model were done on the

remaining 9372 columns. Each column has 6 cortical layers (L2, L3, L4, L5a, L5b and L6). Cortical neurons are modeled using computationally efficient map-based (***Komarov et al., 2018***) spiking PY and IN neurons. Intra-columnar connections follow the canonical cortical circuit (***Figure 1***A), while long-range cortical connectivity (***Figure 1***B) is based on diffusion MRI (dMRI) tractography (***Rosen and Halgren, 2021***) of the Human Connectome Project (HPC) young adult dataset (***Van Essen et al., 2013***), organized into the 180 parcels of the HCP multimodal atlas (***Glasser et al., 2016***)). The originating and terminating layers of long range connections are assigned according to the parcel's relative hierarchical positions (***Figure 1***D-E). Column-wise connectivity is obtained by applying the parcel-wise relation between connection length and probability to synthesized intercolumnar distances (***Figure 1***C, see Diffusion MRI Guided Connection Probability for details). The resulting connectivity (***Figure 1***G) retains the parcel-wise structure from the data (***Rosen and Halgren, 2021***) (***Figure 1***F) , with an approximately exponential distribution between connection frequency and length (see ***Figure 1***C). The connection delays, which are proportional to the geodesic connection lengths, follow a similar distribution. The thalamus is simulated with layers of thalamocortical (TC) and reticular thalamic (RE) neurons (***Bazhenov et al., 1998a***,b, ***2002***), and consists of the core and the matrix (***Bonjean et al., 2011***, ***2012***), which selectively project to the neurons from different cortical layers satisfying the outlined cortico-thalamo-cortical loop (***Shepherd and Yamawaki, 2021***). Following (***Krishnan et al., 2016***) the model included the effects of neuromodulators to induce transitions between Wake state and SWS.

In the following sections, we first discuss "baseline" awake and sleep state dynamics of the model and then we discuss effects of alternating network connectivity on SWS. We then present analysis of human recordings and compare different model dynamics to human data using coherence analysis across frequency and distance. In addition to the basic characteristics of SO frequency, amplitude, and propagation speed, network effects are primarily described in terms of 3 key metrics: *synchrony*, *spread*, and *participation*. Synchrony refers to the timing of the Up state onsets and offsets across all neurons participating in a slow wave. Spread refers to how far the slow wave travels across the cortex. Finally, participation refers to the percent of neurons that participate in the slow wave within the area of spread.

Wake State Characterization

Wake state (***Figure 2***A) was tuned to show a consistent average firing rate of individual neurons at about 17 Hz. The power spectral density (***Figure 2***a.5) revealed a distinct $1/f$ phenomenon, as is common for in vivo recordings in awake state (***Donoghue et al., 2020***). Individual neurons showed irregular tonic firing (***Figure 2***a.1), with baseline membrane voltage around -65 mV (***Figure 2***a.4). The firing activity was not synchronized (***Figure 2***a.3), which was reflected in the low voltage LFP (***Figure 2***a.2). Overall, the network revealed properties representative of biological wake state activity.

Slow Wave Characterization

To attain a network displaying SWS-like activity from the wake state baseline, several cellular and neurochemical parameters were adjusted according to the methodology presented in (***Krishnan et al., 2016***). Namely, we increased cortical AMPA and GABA conductances as well as cortical leak and slow hyperpolarizing currents in all cortical neurons (see Methods, ***Table 4***).

The resulting baseline model of SWS (***Figure 2***B) revealed synchronized and regular oscillations (~0.27 Hz) between silent (Down) and active (Up) states (***Figure 2***b.2) in all cortical excitatory and inhibitory neurons (***Figure 2***b.1). This network dynamics was organized as the waves of spiking activity propagating across the entire cortex - slow-waves. This can be seen in Supplemental Video S1. The slow-waves were further highly synchronized across layers (Supplementary ***Figure S1***). In general, the network spent more time in the Down states, and the Up state onsets and offsets were well synchronized (see narrow onset and offset histograms in ***Figure 2***b.5). This pattern is typical for recordings under urethane anesthesia (***Steriade et al., 1993a***), while Down states may be shorter in

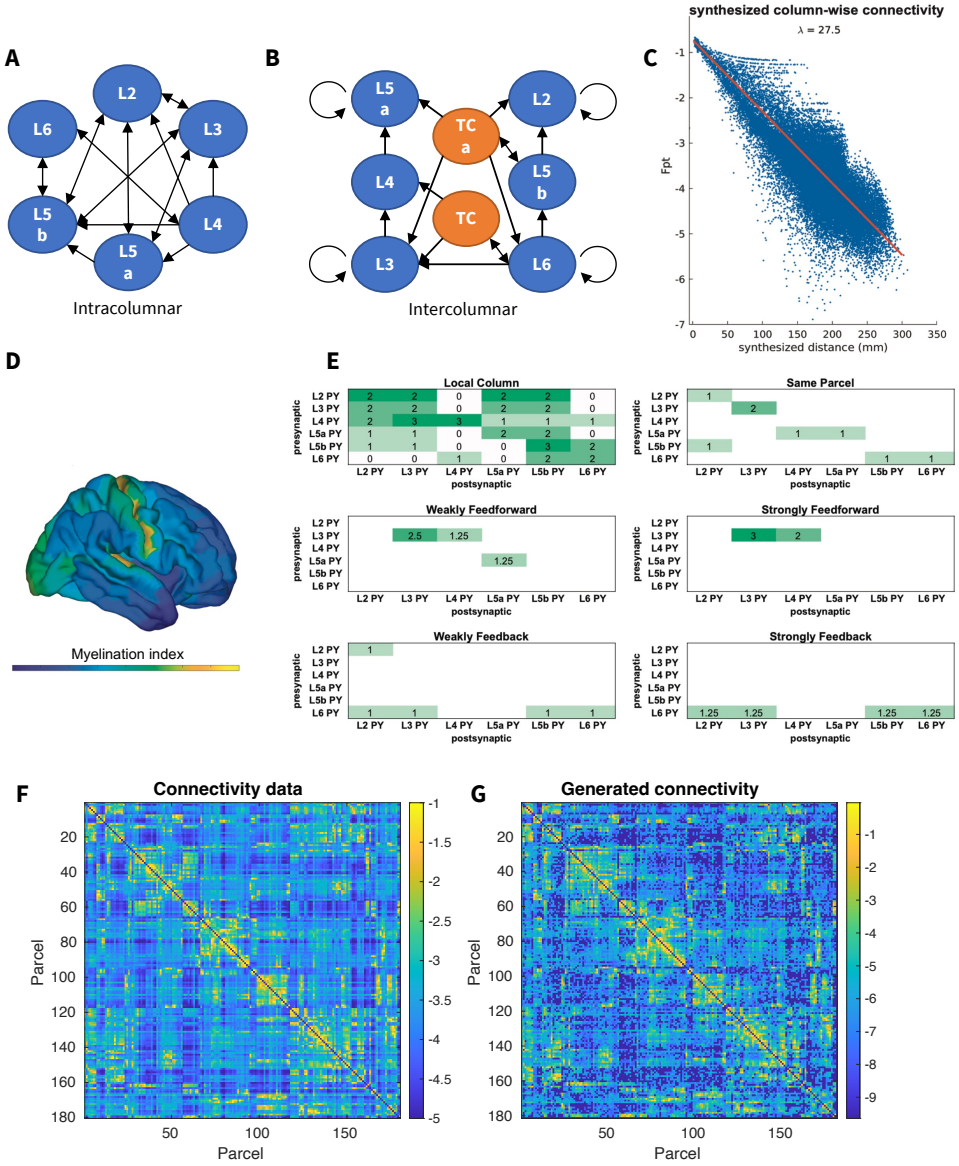

Figure 1. Model architecture. A) Connectivity between neurons in the same column follows the canonical circuit. Arrows indicate directed connections between layers. Neurons are never connected to themselves. B) Connectivity diagram between different cortical columns and thalamocortical cells in the core (TC) or matrix (TCa). C) Exponential decay of connection probability with distance between columns. Previously reported inter-parcel dMRI connectivity (***Rosen and Halgren, 2021***) shows an exponential relation with fiber distance. Column-wise connection probability is obtained by applying the dMRI exponential function to inter-column fiber distances (synthesized from their corresponding geodesic distances) and then adding the residual inter-parcel dMRI connectivity, estimated by regressing out the exponential trend (see Diffusion MRI Guided Connection Probability for details). D) Estimated myelination index (***Glasser and Essen, 2011***; ***Burt et al., 2018***) throughout the cortex. A hierarchical index inversely proportional to this myelination index is assigned to each of the 180 cortical parcels designated in the HCP-MMP atlas (***Glasser et al., 2016***). E) Excitatory corticocortical connections belong to one of 6 classes based on the hierarchical index of the pre- and post-synaptic neurons: within the same column, within the same parcel, weakly or strongly feedforward (from lower to higher hierarchical index) and weakly or strongly feedback (from higher to lower hierarchical index). Based on experimental reports on connectivity (***Markov et al., 2013***; ***Rockland, 2019***) weights are scaled according to the connection type by the factor shown in the matrices. F) Parcel-wise connectivity from ***Rosen and Halgren*** (***2021***). G) Generated model connectivity, which approximately reproduces the parcel-wise structure from data in panel F.

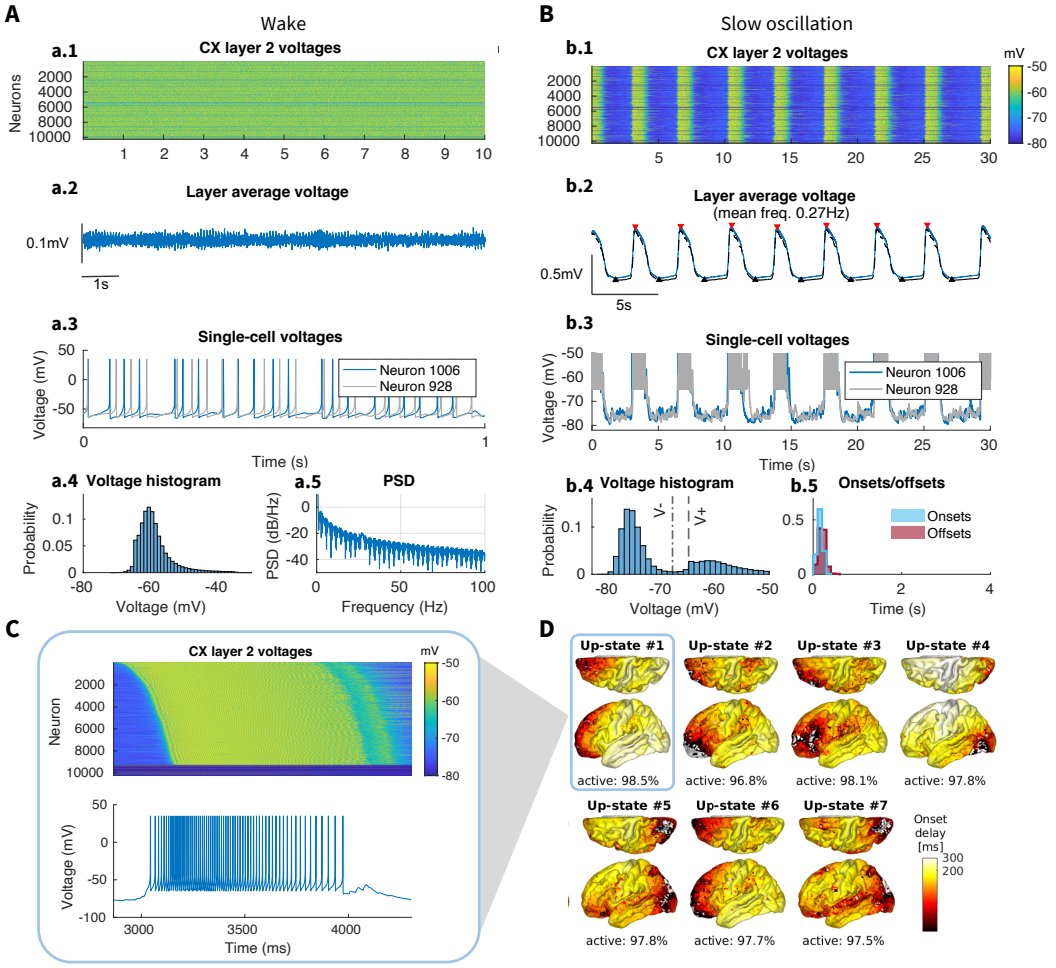

Figure 2. Baseline model activity in wake and sleep states. A) Wake state. a.1) Membrane voltages of all neurons from layer 2 over 5 seconds of simulation; a.2) Layer average voltage over time, simulating LFP; a.3) Activity of two representative neurons from layer 2, both showing irregular tonic firing; a.4) Voltage histogram of all neurons over the whole simulation time, note -65mV peak representing baseline membrane voltage; a.5) Power spectral density (PSD) of the average voltage revealed a distinct $1/f$ phenomenon typical of *in-vivo* recordings. B) Slow-wave dynamics. b.1) Membrane voltages of all neurons (including medial wall) from layer 2 over 30 seconds of simulation, revealed synchronized bands of activity during Up states; b.2) Average voltage of all cortical layers over time (*dashed black line*) and layer 2 average voltage over time (*solid blue line*, excluding medial wall), with nearly identical behavior. *Red* and *black triangles* mark global Up and Down states from layer 2; a.3) Activity of two representative neurons from layer 2, both showing synchronized activity during each upstate; a.4) Voltage histogram of all neurons over the whole simulation time, revealed the characteristic bi-modal distribution caused by Up and Down state alternations during SWS. Dashed vertical lines labeled V^- and V^+ indicate the voltage thresholds used to detect Down states and Up states, respectively; b.5) Distribution of the Up state onsets and offsets for all neurons over the whole simulation time. Narrow histograms indicate highly synchronous initiation and termination of the Up states. C) Zoom into the first Up state from panel b.1, with neurons sorted from earliest to latest onset time, and a single cell voltage from panel b.2, showing the transition from Down to Up state, steady firing during the Up state, and transition to Down state. D) Latency map, calculated as the onset delay of each neuron with respect to the earliest onset, for each Up state in panel b.2 (see Onset/offset Detection in Methods for details). The percent of active neurons during each Up state is shown below the corresponding latency map. Up-states involve nearly every modeled neuron in the cortex within 300ms from its initiation time. Moreover, a single initiation site is generally identifiable, with activity spreading progressively to farther regions of the cortex in the manner of a travelling wave.

non-anesthetized animals (***Steriade et al., 2001***). Nevertheless, the frequency of SOs was within the range of human data (***Csercsa et al., 2010***). The latency maps in ***Figure 2***D demonstrate how waves of activity travel from a single initiation site, which varied between Up states with no detectable dependency on the previous ones, in about 300ms. Each Up state involved >97% of all excitatory neurons. In this baseline model, slow-waves revealed both high spread and high participation. Cortical inhibitory, thalamocortical, and reticular thalamic neurons all showed similar pattern of oscillations (Supplementary ***Figure S2***), as previously shown in (***Bazhenov et al., 2002***).

Connection Density

In the baseline model, connections between neurons were set to match biological data (see Methods). Next, to test the effects of connection density between regions, we gradually changed the density of connections, by applying a probability P to retain each possible connection (***Figure 3***A-B) regardless of the distance between neurons, thus keeping the connection distance distribution unchanged (***Figure 3***C). Strengths of remaining synaptic connections were scaled up to compensate for the lost connections to ensure an equivalent amount of net activation per neuron in the network (see Methods for details).

Setting the probability from 100% down to 50% (i.e., ablating a random half of all connections) had minimal effect on the slow waves, indicating the model's robustness to even significant loss of individual connections as long as the total strength of excitatory synaptic input per neuron remains unchanged. Slow waves exhibited a similar propagation pattern with only a slightly reduced amplitude (approx. 92% of baseline SOs) and speed (***Figure 3***D, F). The synchrony of the Up state offsets, however, was impaired; the distribution of offset timings across neurons became much wider (***Figure 3***d.5, f.5) compared to baseline model (***Figure 2***b.5). Further decreasing density below 30% caused a considerable drop in amplitude and participation (***Figure 3***f.1, f.4). In the extreme case of only 10% of connections remaining ($P = 0.1$, ***Figure 3***E), there was continued loss of synchrony in Up state offsets and onsets, slow waves became less frequent (down to 0.17 Hz), with lower amplitude (50% of baseline), and lower participation (only 70% of neurons involved per upstate) (***Figure 3***F). Nevertheless, slow waves still propagated through the all brain regions on the macro scale, showing that long range synchrony is still possible (if slightly impaired) with only very few connections in place as long as those connections are sufficiently strong and long-range connections are present. Below this level of remaining connections, slow waves no longer occurred and the network was largely silent.

Figure 4 shows further details into the slow-wave dynamics in the case of extreme density loss ($P = 0.1$), zooming into ten cortical regions with a 5mm radius each (***Figure 4***A). Single cells and LFPs in different regions throughout the cortex (***Figure 4***C-D) showed synchronized Up states, although many neurons were not active during individual Up states (***Figure 4***C, E). The local heterogeneity in activation patterns induced by the extreme sparsity of connections is evident in ***Figure 4***E, which shows many silent neurons in the immediate vicinity of active cells. This generated the extremely granular participation seen in the latency maps (***Figure 4***F). Even though each Up state encompassed cells in the whole cortex (high spread), a large fraction of cells distributed through the entire cortex did not participate in slow-waves (decreased participation). This model can further be seen in Supplemental Video S2. Initiation was diffused with respect to the baseline simulation, to the point where a single meaningful estimate of propagation speed for each Up state could no longer be computed.

Connection Range

To determine the specific contribution of long-range connections, we varied the maximum connection radius; any connections longer than a specified distance R were set to 0 (***Figure 5***A). Again, the strengths of remaining connections were scaled up to compensate for reduction in the total number of connections and to keep total synaptic input per cell unchanged. In contrast to the density reduction (see ***Figure 3***C), this alteration did shift the connection distance distribution (***Figure 5***C).

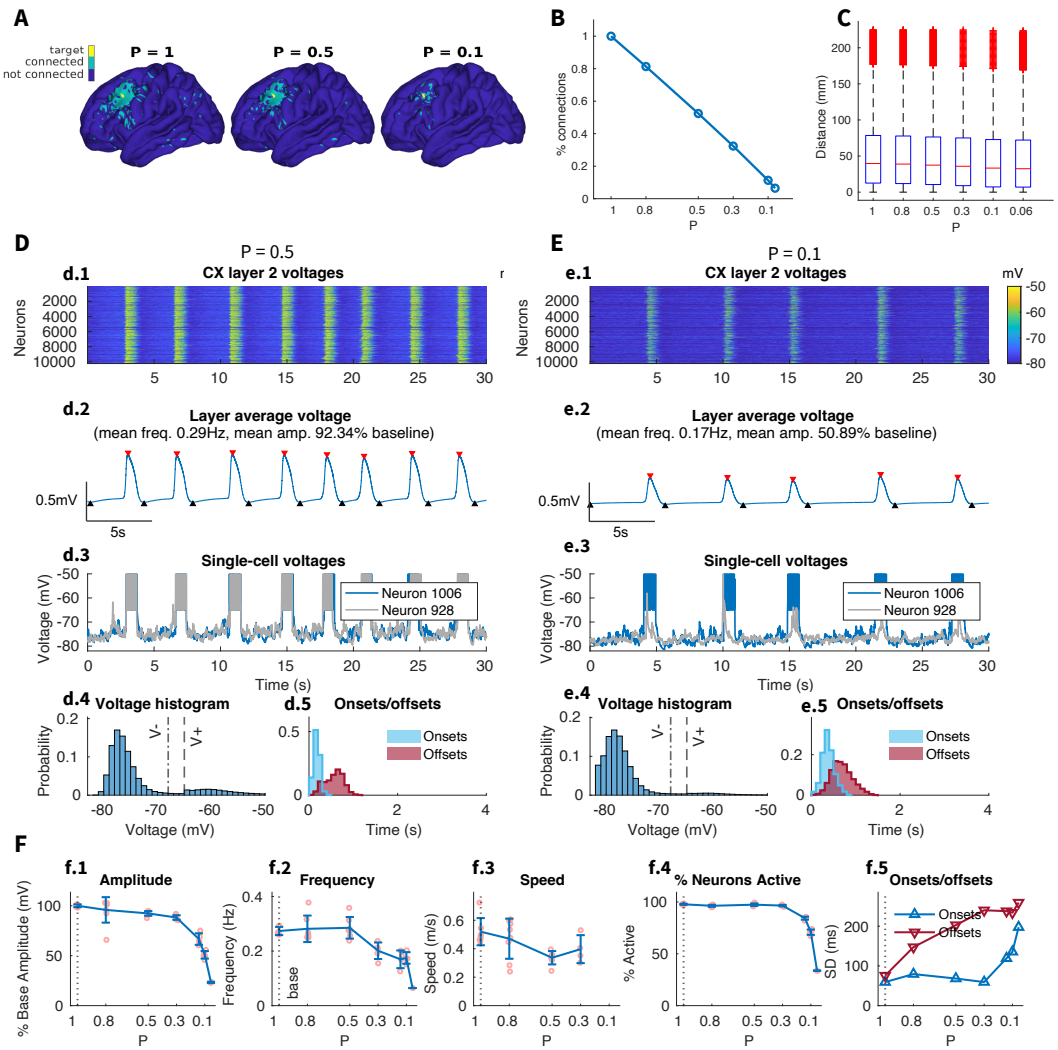

Figure 3. Effect of connection density on SO dynamics. A) Example target cortical column (*yellow*) with all columns connected to it through any layer (*green*) for different connection densities. Density is reduced by decreasing P, which denotes the probability of preserving a connection from the original dMRI-based connectivity. With $P = 1$ all connections are preserved, while for $P = 0.5$, $P = 0.3$ and $P = 0.1$ each connection is preserved with a $50\%, 30\%$ or 10% probability, respectively. B) Percent of the original number of connections retained for different values of P. C) Distribution of connection distances, or lengths, for different values of P. Red horizontal lines indicate medians, bottom and top box edges indicate the 25th and 75th percentiles, respectively, whiskers extend to the most extreme data points not considered outliers, and outliers are plotted individually using the '+' marker symbol. Note, connection density is reduced uniformly across all lengths. D-E) Individual analysis of SO dynamics for different values of P. Subpanels as in ***Figure 2***. F) Summary of the effect of reducing connection density on the global SO frequency and amplitude as well as the standard deviation of the onset/offset delays (i.e. the width of the onset/offset histograms in d.5 / e.5)

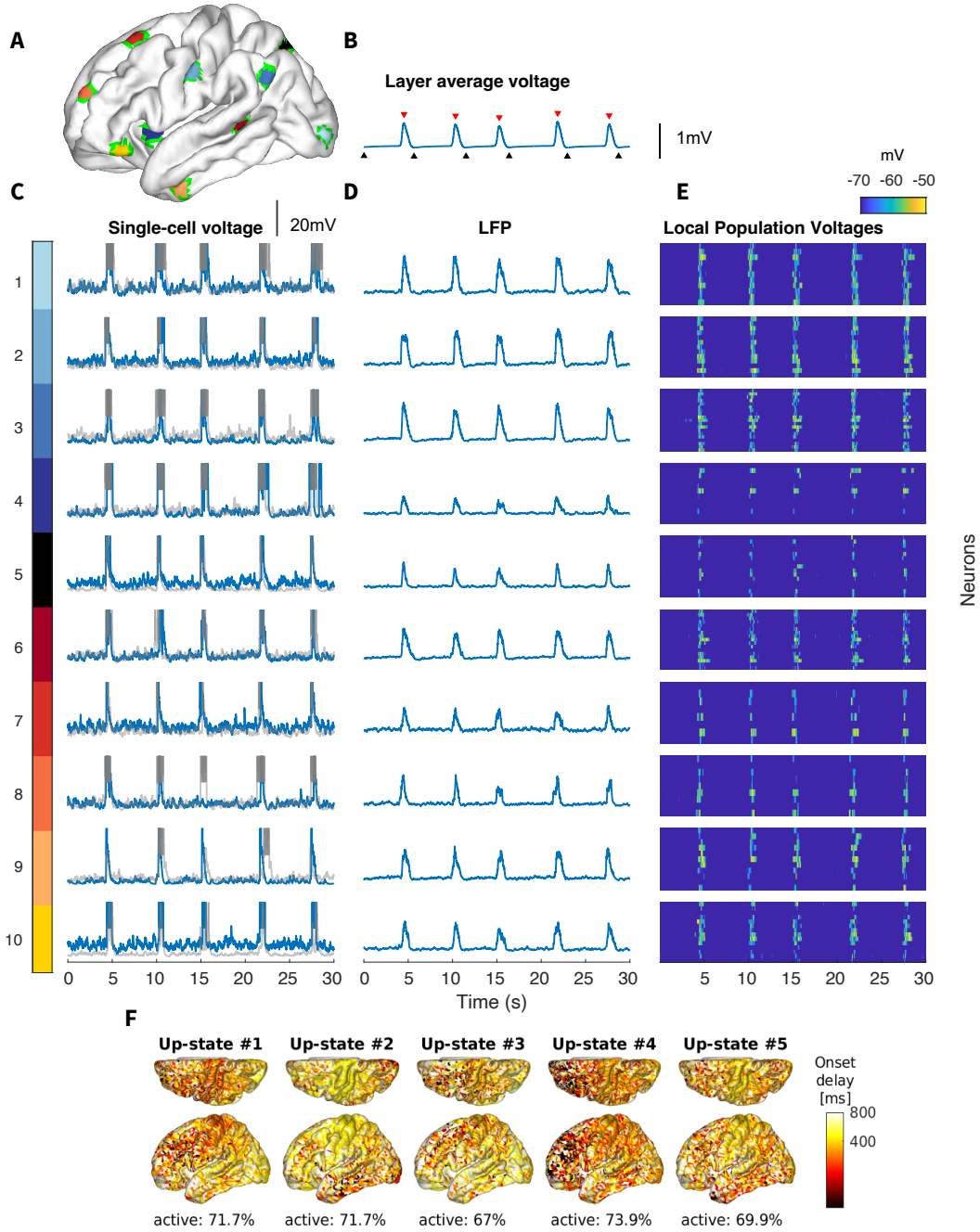

Figure 4. Local activity for $P = 0.1$, with 90% connections removed. A) Ten cortical areas with a 5mm radius, that were used to calculate local dynamics. B) Average membrane voltage of layer II neurons, as in ***Figure 3***e.2. C-E) For each region in (A), subpanels show: (C) the single-cell voltage for two neurons in the area , (D) the local field potential (LFP) for the 5mm area, and (E) heatmap of individual voltages of all neurons in the area. Up states are largely synchronized across all 5 regions. F) Latency map for each upstate in the $P = 0.1$ simulation. Even with very sparse connectivity, Up states spread to the whole cortex. Participation was reduced uniformly to about 70% compare to nearly 100% participation when all connections are present (compare to ***Figure 2***D)

The maximum connection length in baseline model was 226.1 mm, but most connections (approximately 80%) were maintained within 100 mm (***Figure 5***B). A connection radius as small as 5 mm, which includes second-order neighbors of a given neuron, resulted in only approximately 10% of connections still intact. The alterations of the maximum connection length led to significantly different activity patterns than in the network with a spatially uniform drop to the same percentage of connections (Connection Density). The network with a maximum connection radius of 5 mm (***Figure 5***D) showed no reduction in the frequency of the slow waves, but both the onsets and offsets of the slow waves revealed dramatic reduction in synchrony. Additionally, there was a substantial drop in slow wave propagation speed, while changes in connection density had minimal effect on speed (compare ***Figure 5***F and ***Figure 3***F). Despite all this, characteristic properties of global slow waves (high spread and high participation) found in the baseline model were maintained.

However, reducing radius below 5mm (i.e., not including 2nd degree neighbors) caused a dramatic drop in global oscillation amplitude, akin to a phase transition from global to local oscillations. With a connection radius of 2.5 mm (***Figure 5***E), including only first order neighbors of each cell, global slow waves were lost in favor of local slow waves in small regions of the cortex (***Figure 6***, low spread, high participation). Note that this radius retains only 3.7% of connections, where a spatially uniform drop to any less than 10% of connections removed slow waves entirely. These local slow waves were generated in multiple initiation sites simultaneously, and occasionally showed regional propagation but never travelled across the full hemisphere (***Figure 6***F). This resulted in reduced global SO amplitude as long-range synchrony between locally oscillating neural populations was impaired (***Figure 6***C-D). This model can further be seen in Supplemental Video S3. While a large fraction of the cortex was not participating in SO, the active regions (such as region 6, ***Figure 6***) were consistent across Up states. A connectivity analysis revealed that these regions correspond to the network areas with the highest node degree (see Supplementary ***Figure S4***). The same regions exhibited local slow waves for different simulations with the same connectivity parameters but different random seeds for network generation. This means that the active, i.e., generating local SO, areas are not random, but instead emerge from the underlying structure imposed by the dMRI connectivity data.

On the contrary, setting a minimum (rather than maximum) radius of up to 10 mm resulted in global slow waves that retained synchrony (not shown). In contrast to previous simulations, the initiation zones were here seen to resemble the edges of a circle and spread out, with silence in the epicenter: the lack of local connections made slow waves that "skip over" the most local regions to the initiation zone. An extreme case of 100 mm minimum radius (80% of connections removed) resulted in no defined initiation zone, but rather synchronized slow waves with diffuse initiation across the cortex.

As a whole, this analysis revealed that long range connections (longer than 5 mm) are essential for the large-scale synchrony of the slow waves, but having only local connections (less than 5 mm) is still sufficient to make slow waves propagating over entire cortex (as long as remaining connections strength is scaled up to maintain total synaptic input per cell). Even with only first order neighbors, the network still maintained slow wave initiation, synchrony, and participation with local propagation.

Connection Delay

The model implements synaptic delays scaled by geodesic distance between neurons with a maximum delay of 40 ms. The delay for the majority of synapses is under 2 ms because the vast majority of connections are relatively short range. To test the effects of delay times, we changed the delays in two ways (***Figure 7***): 1) by changing the maximum delay and scaling all others proportionally, and 2) by setting one uniform delay to all connections.

Setting the maximum delay to be smaller (all the way down to 0.1 ms) had little to no effect on slow wave amplitude, frequency, or synchrony. Setting the maximum delay to be larger also had minimal effect on network activity until biologically implausible delays were implemented (≥1

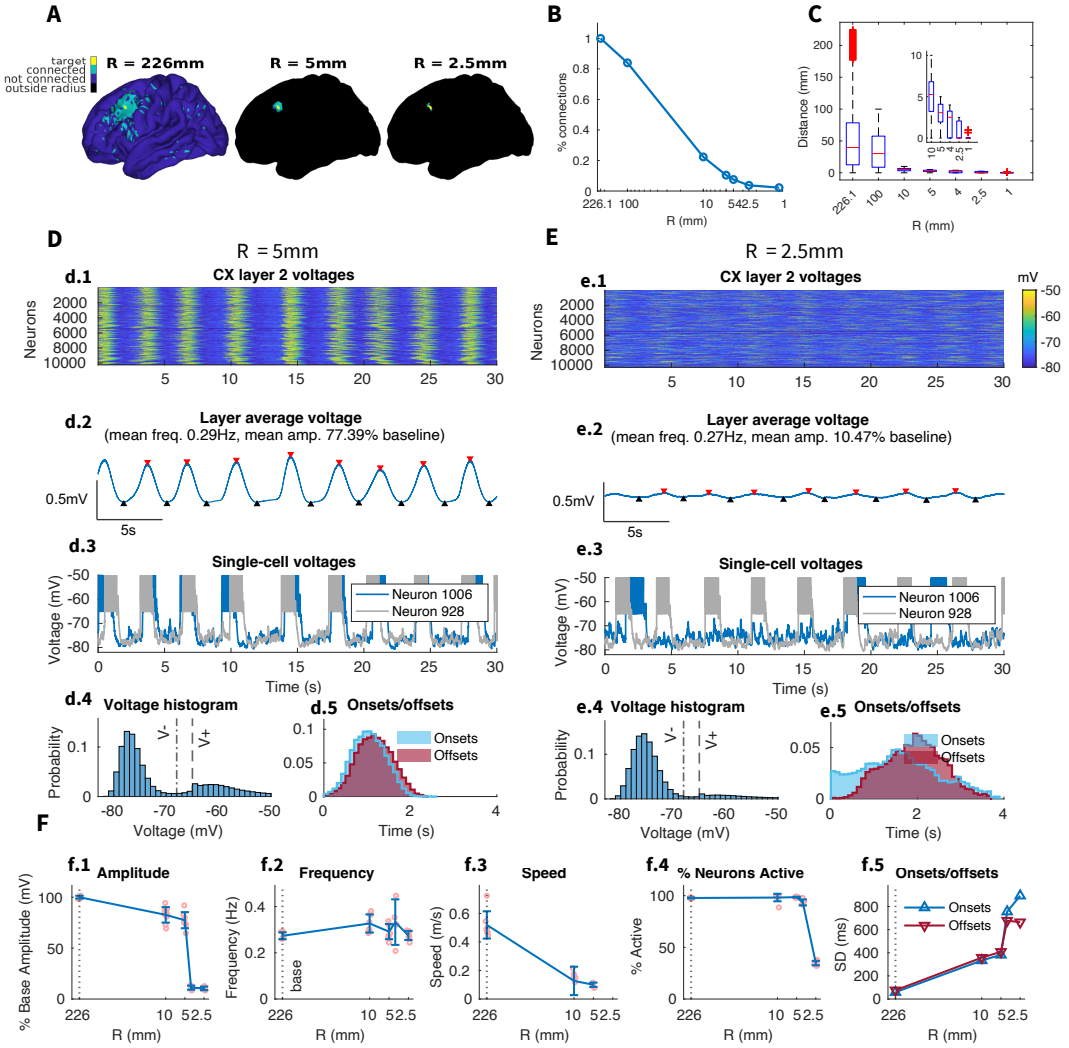

Figure 5. Effect of connection range on SO dynamics. A) Example target column (*yellow*) with all its connected columns (*green*). The *blue* area indicates the connection range for the corresponding radius R. No connections are made in the *black* region outside the radius. $R = 226mm$ encompasses all the original dMRI-derived connections. B) Percent of the original number of connections preserved for different values of R. C) Distance distribution for different values of R, with *inset* zooming into radii below 10mm. R imposes a maximum connection length and truncates the distance distribution accordingly. Red horizontal lines indicate medians, bottom and top box edges indicate the 25th and 75th percentiles, respectively, whiskers extend to the most extreme data points not considered outliers, and outliers are plotted individually using the '+' marker symbol. D-E) SO analysis for $R = 5mm$ and $R = 2.5mm$. Subpanels as in ***Figure 2***. F) Summary of the effect of reducing connection density on the global SO frequency and amplitude as well as the standard deviation of the onset/offset delays (i.e. the width of the onset/offset histograms in d.5 / e.5)

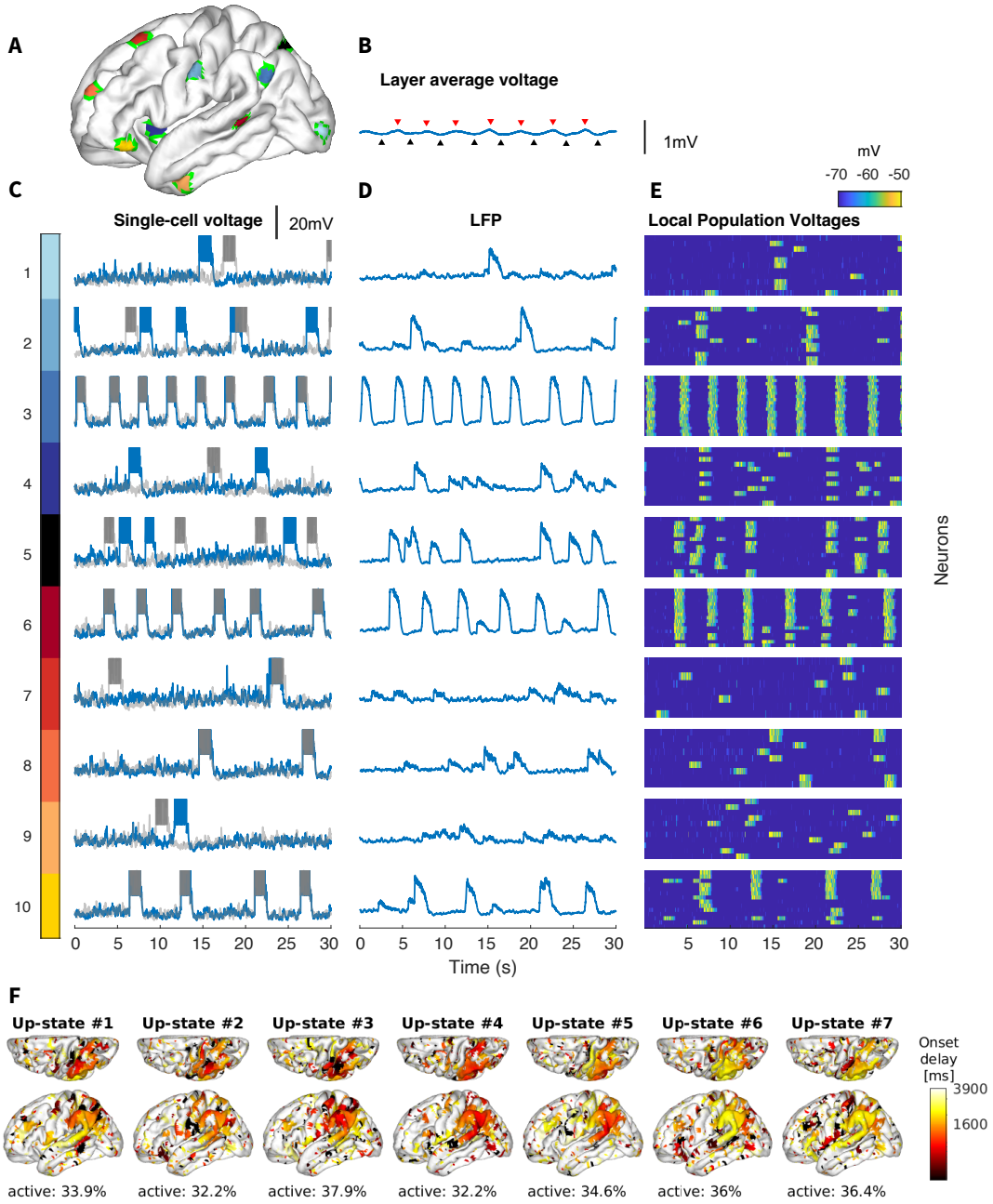

Figure 6. Local SO for small connection radius ($R = 2.5$mm). A) Ten cortical areas with a 5mm radius, that were used to calculate local dynamics. B) Average membrane voltage of layer II neurons, as in ***Figure 5***e.2. C-E) For each region in (A), subpanels show (C) the single-cell voltage for two neurons in the area, (D) the local field potential (LFP) for the 5mm area, and (E) heatmap of individual voltages of all neurons in the area. Note that even within these very small regions, there are still subgroups of independently synchronized neurons. F) Latency map, calculated as the onset delay of each neuron with respect to the earliest onset, for each upstate identified in ***Figure 5***e.2. Note that even the most global of slow waves has very low participation, around 35%, and can be seen to consist of many extremely small initiation sites that generally do not spread.

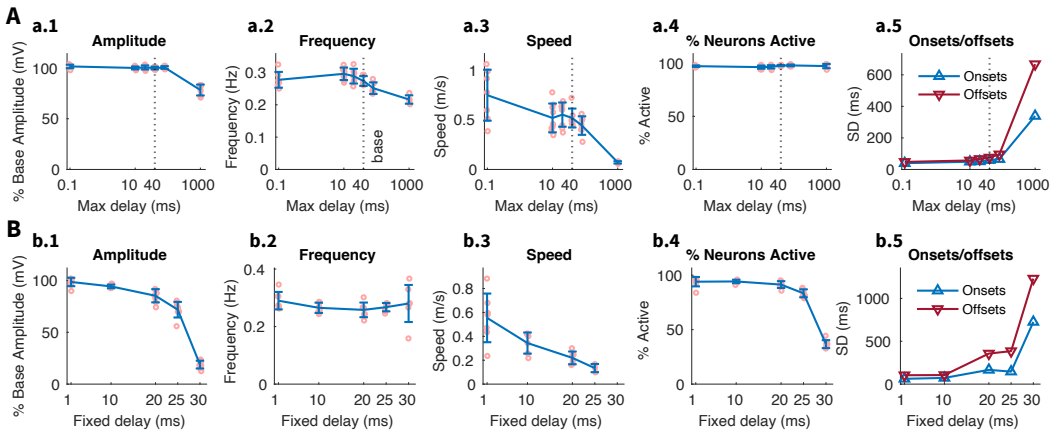

Figure 7. Effect of Synaptic Delay, either via setting a uniform delay (A) or scaling the max delay (B) on SO dynamics. (A and B) Summary plots of frequency, amplitude, and onset / offset spread. Decreasing the max scaled delay to 0.1 ms (from 40 ms) has no effect, while increasing the max scaled delay up to 1 second shows only minor changes in frequency frequency and amplitude but notably increased onset/offfset synchrony. Low uniform delays similarly showed no effect, with loss of amplitude and synchrony only seen at 30 ms (most delays were previously under 2 ms).

second). Even at this extreme the network retained strong global slow waves, albeit with slightly lower amplitude, longer frequency, and de-synchronized onsets and offsets. Setting a uniform delay of 10 ms (where most delays were previously under 2 ms) further left the network behavior largely unchanged. Only when the uniform delay was increased to 30 ms did we observe a loss of amplitude and synchrony (***Figure 7***). Since the delay times here shown to have an effect on network behavior are clearly beyond the range of biological plausibility, these results indicate that synaptic delays are not a primary determinant of slow wave spatio-temporal properties.

Connection Strength

To probe the effects of absolute connection strength on the network activity, we varied the base connection strength between all cortical pyramidal neurons (***Figure 8***A, C). In contrast to experiments with changing connectivity density or radius, where remaining synapses were scaled to keep total synaptic input constant, this changed the total synaptic input per cell. Weight reductions or increments by a factor of 4 or more caused the slow oscillations to be barely detectable or undetectable (note the low amplitude at the extremes of ***Figure 8***c.1). This was a result of low activity in the case of weights reduction, and of sustained Up state (Down state absence) in the case of weights increase. In general, within the detectable range, the SO amplitude, frequency, and participation decreased when synaptic strength was decreased (***Figure 8***C). Note that the model revealed an overall robustness to weight variation: the slow-wave propagation was minimally altered by strength increases or decreases by a factor of 2.

To further investigate the role of long range connectivity, we next performed N times synaptic weight reductions on only "long-range connections", i.e., connections over a defined minimum radius R_{th} (***Figure 8***B,D). We varied the scaling factor N from 2 to 7 and radius threshold R_{th} from 2.5 mm to 50 mm (***Figure 8***B illustrates the case N=5, R_{th}=10mm). Again, we did not scale the total synaptic input per cell, so these alternations affected balance of excitation and inhibition in the network. This experiment can be interpreted to model the effect of stronger synaptic inputs nearest to the cell body (***Hawkins and Ahmad, 2016***; ***London and Segev, 2001***).

When connections over R_{th}=10mm were significantly weakened (N=5) (***Figure 8***B, ***Figure 9***), the model displayed a number of clearly identifiable local slow waves originating and reliably traveling around the hemisphere in different directions (***Figure 9***F). Occasionally, these local slow waves would coincide to produce a global slow wave in the LFP (see ***Figure 8***b.2, where red downward

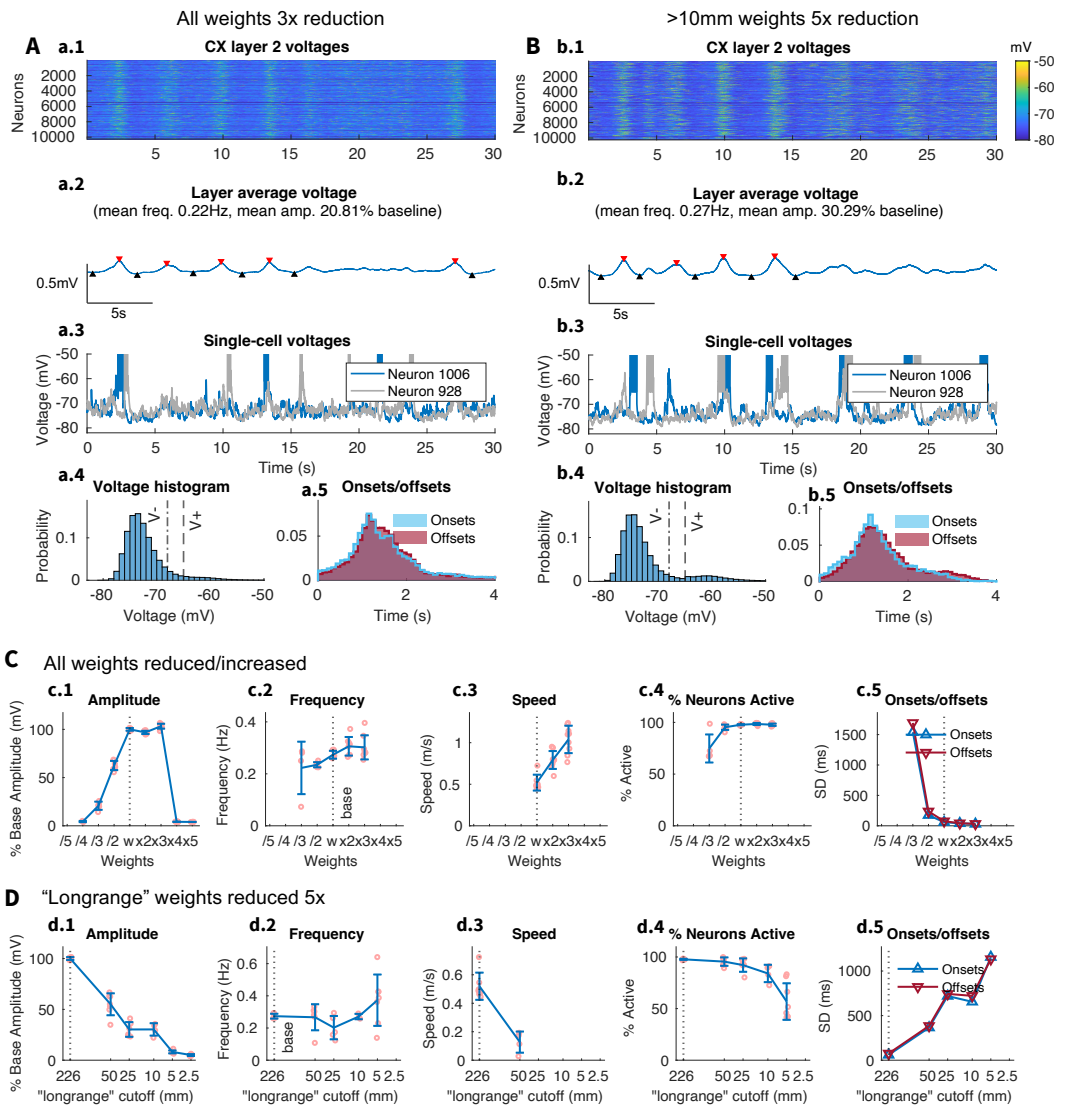

Figure 8. Effect of cortical excitatory synaptic strength on the network dynamics. A) Reduction of all cortical connections by 3x. B) Reduction of only connections longer than 10 mm by 5x. All subpanels as in ***Figure 2***. C) Summary of changes in frequency, amplitude, speed, participation, and onset/offset distribution spread when all connections are reduced as shown in (A). Increasing all weights shows little effect while decreasing all weights shows decreased amplitude and participation, with increases in onset/offset distributions (decreases in synchrony). The frequency of slow waves also becomes more variable. Note, Increasing all weights 5x results in the ablation of slow waves due to constant upstate, i.e., SO characteristics cannot be meaningfully quantified. D) Summary of changes in SO characteristics when only long range connections are reduced as shown in (B). Across all plots, 5 mm is seen to be an inflection point (or "elbow") where network activity changes.

triangles mark the four detectable global UP states analyzed in ***Figure 9***F). In this model, the local populations of neurons would regularly synchronize producing local slow waves but the global synchrony was lost in many cases except for a subset of all events when global slow waves were generated (***Figure 9***B, E). With reduced spread and high participation, the local slow wave behavior resembles the results from simulations with exclusively local connectivity (see Connection Range), but stems from the more biologically plausible assumption of weaker (rather than nonexistent) long range connectivity. Indeed, the propagation patterns in ***Figure 9*** is similar to the proposed pattern of biological sleep including a mix of Type I (global) and Type II (local) slow waves, as suggested by (***Siclari et al., 2014***; ***Nir et al., 2011***; ***Bernardi et al., 2018***; ***Funk et al., 2016***; ***Vyazovskiy et al., 2007***, ***2011***; ***Riedner et al., 2007***). This model can further be seen in Supplemental Video S4.

Importantly, not all the cortical regions were equally likely to generate local slow waves. As in simulations with only local connections, the network areas with the highest node degree (see Supplementary ***Figure S4***) produced almost regular local slow-waves (e.g., region 6, (***Figure 9***)), while some other (e.g., region 9, (***Figure 9***)) displayed low frequency irregular spiking with only rare Up state-like events. This again suggests that the active, i.e., generating local SO, areas emerge from the underlying structure imposed by the dMRI-based connectivity.

Local vs Global Slow-Waves

Given above analysis, we next sought to quantify the global v.s. local nature of slow waves in each model as a function of synaptic strength. For each model, we generated functional connectivity matrices and quantified the percent of functionally connected parcels (connection pairs with a correlation of r >= 0.25). When sorted by the percent of connected units (***Figure 10***A), three clusters can be revealed, one in each third of the range from 0-100% functionally connected. In the top third (greater than 66% of parcels functionally connected), we find models with primarily global (Type I) slow waves; in the bottom third (less than 33% of parcels functionally connected), models exhibit primarily local (Type II) slow waves. Between this range of 33% - 66% functional connectivity, models exhibit a mixed state of both global and local slow waves. This is seen in models with connections longer than 10mm reduced 4x or 5x, or connections longer than 5mm reduced 4x. These results were verified by eye.

We were further interested in whether scaling all synaptic weights of a mixed state model may mediate the transition from global to local slow waves. To test this, we uniformly scaled by 25-50% all weights of the 10mm reduced 5x mixed model or 5mm reduced 4x mixed model. In both cases, increase in all weights led to only local slow waves, while an equivalent decrease showed only global slow waves (***Figure 10***A).

We then asked if these results could simply be explained by the total synaptic strength in each model. We calculated synaptic strength of each model as a percentage of total synaptic strength in the baseline global slow wave model, and plotted the results against functional connectivity. As can be seen in ***Figure 10***B, total synaptic strength does not fully explain differences in functional connectivity. Models with only 10% - 30% of baseline strength may exhibit only global, only local, or both types of slow waves. In particular, the range of mixed and local-only slow wave models nearly entirely overlaps. These results imply that a proper balance between long and short range connection strength is necessary for a mixed slow wave phenotype - importantly, no models with uniform reductions show this capability.

Coherence Analysis

To validate our network models, we conducted a comparative analysis with experimental data. Specifically, we analyzed coherence across 180 cortical parcels. We calculated coherence in successive narrow-band signals across all parcel pairs to generate a snapshot of coherence across both frequency and distance. Subsequently, we fit the results with an exponential model. From this model, we estimated the spatial length constant (λ) and the scaling term (α). These parameters were then used to compare the coherence landscape shapes of different biophysical models

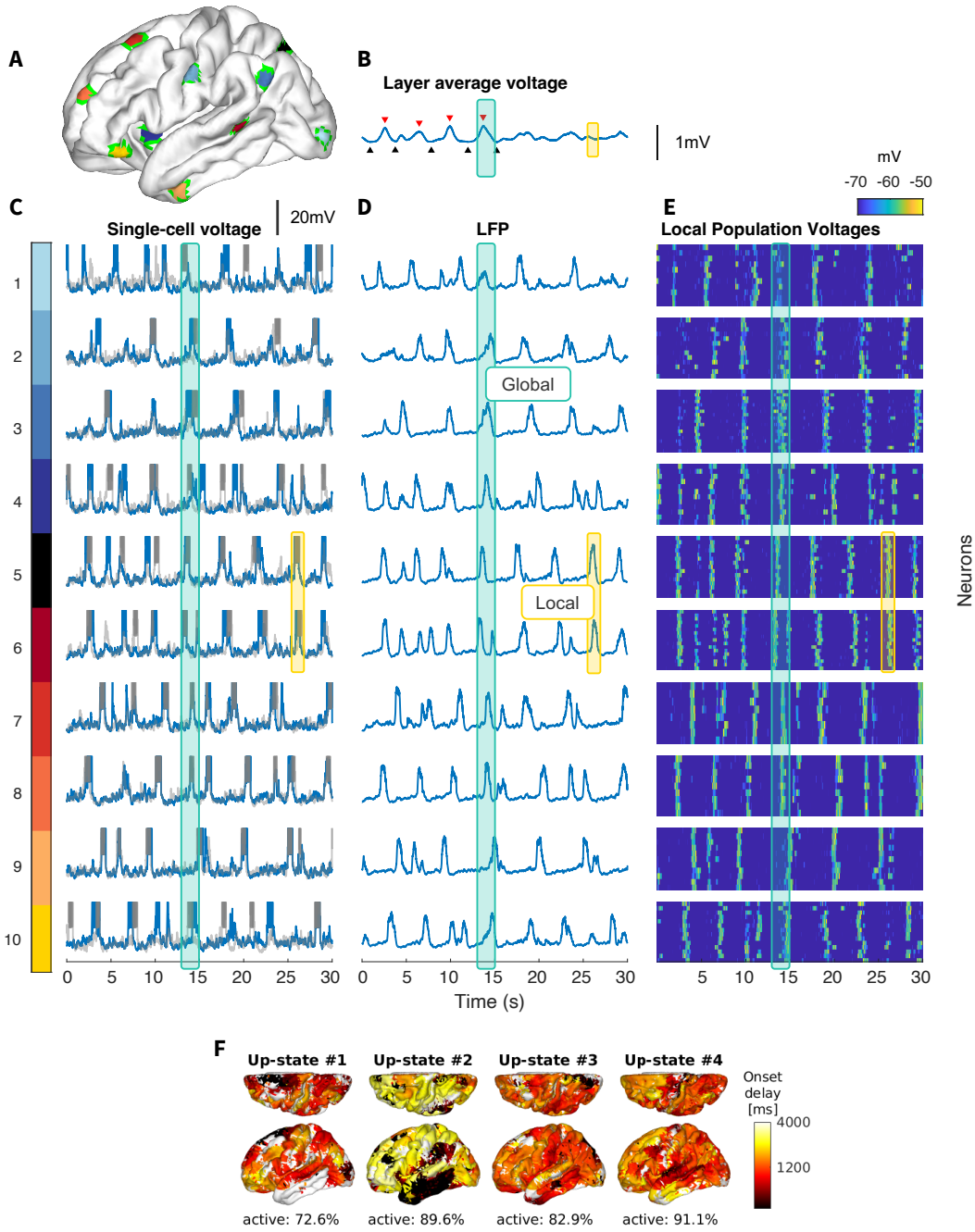

Figure 9. Mixed global (Type I) and local (Type II) Slow Waves: Connections greater than 10mm reduced 5-fold. A) Ten cortical areas with a 5mm radius, that were used to calculate local dynamics. B) Average membrane voltage of layer II neurons. C-E) For each region in (A), subpanels show (C) the single-cell voltage for two neurons in the area, (D) the local field potential (LFP) for the 5mm area, and (E) heatmap of individual voltages of all neurons in the area. This demonstrates that while there is some alignment, up states are not strongly global. F) Latency map, calculated as the onset delay of each neuron with respect to the earliest onset, for each upstate. Note, that while some Up states are global (characteristic examples are marked by blue lines), others are comprised of several independent but coinciding local events (examples are marked by yellow lines).

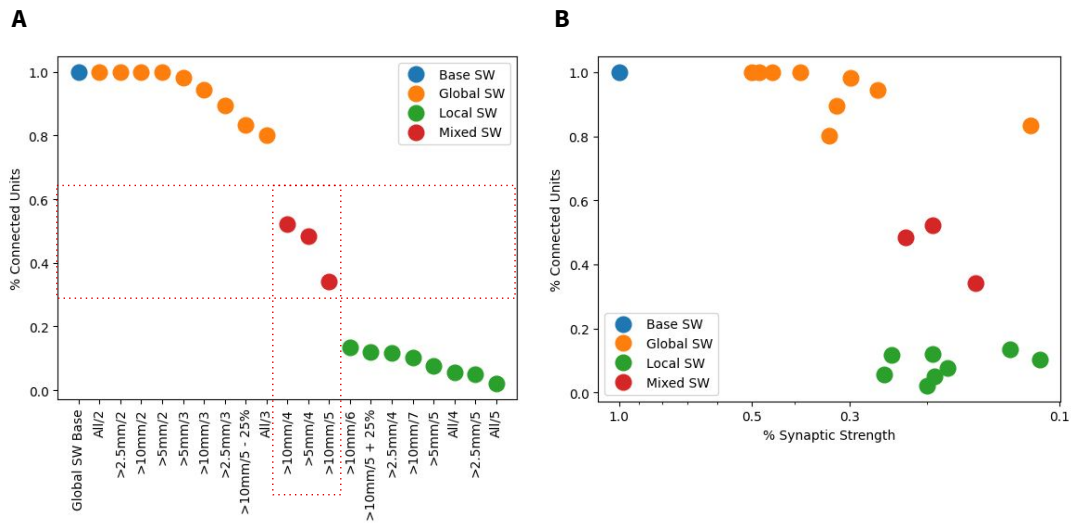

Figure 10. Quantification of Global vs Local Slow Waves. For each model, the percent of connected parcels was calculated using a functional connectivity threshold of r >= 0.25. A) When sorted, the distribution can be seen to cluster into 3 groups along a sigmoid. From this, we classify models by splitting the range into thirds: mostly global slow wave models are classified as having greater than 66% functional connectivity, and mostly local slow wave models with less than 33% functional connectivity. In the middle third, we find models with mixed states of both global and local slow waves. These models are: connections longer than 10mm reduced 4x or 5x, and connections longer than 5mm reduced 4x. B) When plotted against total percent of synaptic strength relative to the global base model, it can be seen that total level of synaptic strength alone is not sufficient to explain differences in functional connectivity. Rather, the ratio of strength in short v.s. long range connections must be considered.

against in vivo data. Full details of coherence analysis can be found in the Methods under Coherence Analysis.

Empirical coherence

The experimental data collection is fully described in Experimental Data. Briefly, continuous stereo-electroencephalography telemetry data were collected for 236 patients with focal epilepsy. After significant data cleaning to ensure removal of epileptic activity and subsequent sleep scoring, NREM sleep data were selected for analysis. ***Figure 11***B shows characteristic coherence landscape obtained in vivo. In ***Figure 11***A, the yellow star indicates the values of λ and α obtained by fitting exponential model.

Model coherence

To perform a comparable model analysis, we first averaged all the cell voltages per parcel (all layers, excitatory and inhibitory neurons) and added noise with signal-to-noise ratio (SNR) = 5 to mimic the signal that would be recorded by a depth electrode, as in experimental data (***Ball et al., 2009***; ***Suarez-Perez et al., 2018***). We then performed coherence analysis in an identical manner to the experimental data.

We compared the exponential fits of the coherence landscapes in the slow wave range (less than 2 Hz) using the mean α and the first λ value (at 0.5 Hz); these two describe the peak coherence and rate of decay. When plotted against each other (***Figure 11***A), the experimental data point can be seen to fall in close proximity to all mixed state models. We found that the global slow wave model, that was initially set as a baseline model, was very far off. The model with all the weights scaled down by factor 3, as well as a range of models with only long range connectivity scaled down by factors 3-5 at the distances above 2.5-10mm, were all within reasonable "distance" (within a factor of 4 in λ and a factor of 2 in α) from empirical data. One could conceive of transitions between

these states occurring as a result of modulation of long range connection strength - for example, the models in which connections longer than 10 mm are reduced 6-fold (local), 4 or 5-fold (mixed) or 3-fold (global) are all relatively nearby the experimental data point. Furthermore, a small (e.g., 25%) increase (or decrease) in all cortical excitatory synaptic connectivity, starting from a mixed-state model, led to exclusively local (or global) slow-wave dynamics and still yielded models with coherence profiles close to the experimental one.

Both the experimental data and the models displaying mixed local/global slow waves (such as a model with a greater than 10 mm reduction, reduced 5-fold) exhibit a sharp peak of coherence at low frequencies, which quickly tapers off with increased distances between parcels (***Figure 11***B,C). Notably, this pattern is not observed in the global slow wave baseline model (***Figure 11***D), where only a slight drop in coherence is seen as the distance between parcels increases. This is expected, given the unrealistic levels of slow wave synchrony across the entire network in this model. Additionally, the global slow wave model shows very high levels of coherence (nearing 1, indicating perfect coherence) at low frequencies. In summary, these results suggest that the coexistence of local and global slow waves requires a specific balance of long- and short-range connection strengths. The models that satisfy this requirement also display coherence profiles matching in vivo data.

Discussion

Traditionally, brain states have been categorized into wakefulness, slow-wave sleep (SWS), and rapid eye movement (REM) sleep, assuming their global occurrence across brain regions. However, recent large-scale neural recordings have revealed the rich heterogeneity of neural dynamics on a brain-wide scale, demonstrating that sleep and wake signatures can coexist in different brain regions, influencing behavior with spatial and temporal specificity. While local circuit mechanisms of slow waves—alternations of positive/negative EEG/LFP waves, also called slow oscillation (SO)—have been sufficiently identified, the factors leading to complex heterogeneous brain states with local slow waves remain unknown. Here, we present a whole-brain thalamocortical network model based on human dMRI connectivity data capable of generating awake states and sleep states with biologically realistic cortical slow waves. The model was applied to make specific predictions about the effects of long- and short-range connectivity on the spatio-temporal dynamics of the slow waves. We identified intracortical synaptic connectivity properties that allow the coexistence of local and global slow waves and proposed mechanisms for transitions between local sleep and global uniform sleep states. The model predictions were compared to human data to validate and fine-tune the models.

A prominent example of brain states heterogeneity is local sleep (***Vyazovskiy et al., 2011***; ***Hung et al., 2013***; ***Quercia et al., 2018***; ***Engel et al., 2016***; ***van Kempen et al., 2021***). During wakefulness, local groups of cortical neurons tend to fall silent for brief periods, as they do during SWS. Furthermore, during behavioral sleep, transient local wake-like activity can intrude SWS (***Nobili et al., 2011***; ***Peter-Derex et al., 2015***). It is worth noting that SWS and REM sleep can also coexist in different cortical areas (***Soltani et al., 2019***; ***Funk et al., 2016***; ***Bernardi et al., 2018***). Additionally, the proportion of time allocated to wakefulness, SWS, and REM states varies significantly across cortical areas (***Soltani et al., 2019***; ***Nazari et al., 2023***), highlighting the diverse predisposition of different regions to support these states.

From mechanistic perspective, the basic need for local sleep can possibly be explained by homeostatic sleep pressure, that accumulates throughout the day, shaped by the duration and quality of preceding alertness. This pressure is evident in the intensity of SWS in the cortex, indicating the brain's need for recuperation (***Wilckens et al., 2018***). Homeostatic sleep pressure can influence cortical functions in specific areas (***Siclari and Tononi, 2017***). For example, spindles and slow waves may intensify in regions engaged in learning (***Eschenko et al., 2006***; ***Pugin et al., 2015***), suggesting that sleep pressure is regulated based on recent cognitive activities. Notably, after motor skill training, there can be a localized increase in SWS within the motor cortex during rest (***Huber et al.,***

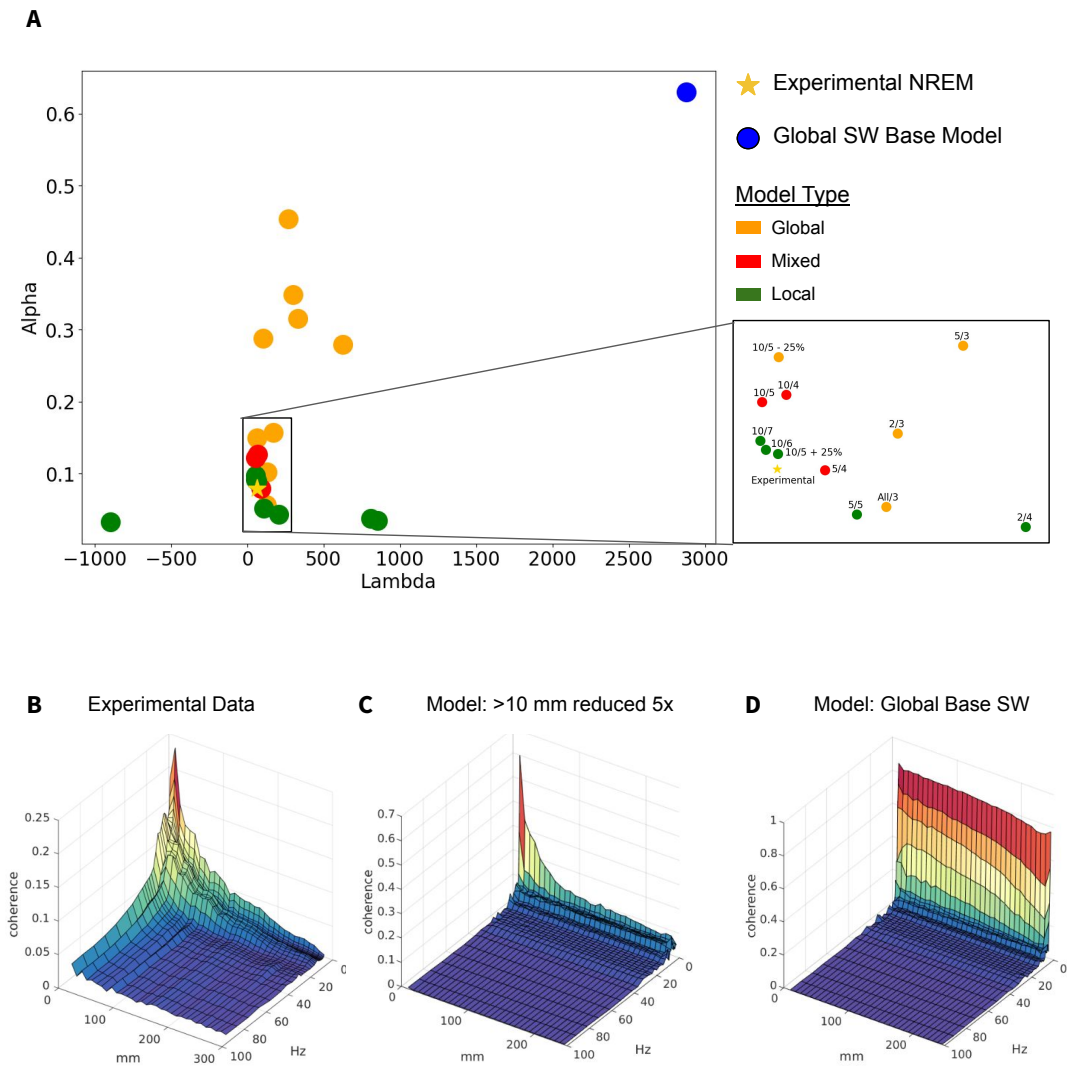

Figure 11. Coherence Analysis of Experimental v.s. Model data. Coherence analysis is performed on all data sets according the the procedure described in Coherence Analysis. The resultant first (0.5 Hz) Lambda and mean Alpha in the slow wave range (<2 Hz) are taken to describe the shape of the coherence landscape, and plotted in (A). The labels refer to the length of long range connections and the strength reduction - i.e., 10/5 indicates a model where connections longer than 10 mm are reduced by a factor of 5. This shows that models with primarily local or mixed local/global slow waves are the closest fit to experimental result. Full 3D coherence plots across distance and frequency are shown for the experimental data (B), the 10mm / 5 model (C), and the global slow wave base model (D), showing that the global slow wave model has a fundamentally different shape (lacking a dependence of coherence on distance) and much higher levels of coherence at low frequencies.

	Density ⇓	Radius ⇓	Delay ⇑	Strength ⇓	Long Range Strength ⇓
Frequency	⇓	-	↓	⇓	-
Amplitude	⇓	⇓	↓	⇓	⇓
Speed	-	⇓	-	-	⇓
Synchrony	⇓	⇓	↓	⇓	⇓
Participation	⇓	-	-	-	-
Spread	Global	Local	Global	Global	Local

Table 1. Summary of results for each network manipulation. Decreasing connection density resulted in decreased slow wave frequency, amplitude, synchrony, and spread, but slow waves remained global. Decreasing connection radius resulted in decreased slow wave amplitude, speed, participation, and spread. Increasing delayed resulted in effects are seen only for manipulations far past biological plausibility, as indicated with a single down arrow for frequency, amplitude, and participation. Decreases in synaptic strength caused reduced amplitude, synchrony, frequency and participation. Finally, decreasing the strength of only long range connections resulted in traveling local slow waves with decreased amplitude, speed, and synchrony.

2004; ***Korman et al., 2007***; ***Hanlon et al., 2009***), and a visual perception learning task can lead to a rise in the initiation of slow waves in the lateral occipital cortex (***Mascetti et al., 2013***).

Why brain areas that are more actively involved in sensory processing during the day require more SWS is a challenging question. We can speculate that it may be related to the well-characterized function of SWS in memory consolidation (***Rasch and Born, 2013***). The slow oscillation (SO) repeatedly resets the thalamocortical network during the Down phase and temporally groups sleep spindles, which are associated with long-term potentiation (LTP)-like processes and learning, during the Up phase (***Mölle et al., 2009***; ***Rosanova and Ulrich, 2005***). These observations have led to the hypothesis that SO provides a global temporal frame within the cortex and between brain regions (e.g., hippocampus, thalamus, striatum) for offline memory processing and reactivation through the strengthening of neuronal circuits (***Isomura et al., 2006***; ***Ji and Wilson, 2007***; ***Pfaff et al., 2008***; ***Rasch et al., 2007***; ***Wierzynski et al., 2009***). Local sleep may thus enable cortical networks to augment memory consolidation in specific brain regions that need it the most.

While specific mechanisms of slow-wave sleep (SWS) generation have been explored in many local circuit models (***Timofeev et al., 2000***; ***Bazhenov et al., 2002***; ***Compte et al., 2003***; ***Hill and Tononi, 2005***; ***Destexhe, 2009***; ***Crunelli and Hughes, 2010***; ***Levenstein et al., 2019***), only a few very recent studies (***Cakan et al., 2022***; ***Goldman et al., 2023***) have proposed simulating realistic long-range cortical connectivity to test its effect on the spatio-temporal properties of SO. While these models take an important step in utilizing global brain connectivity data to study SWS, they apply a mean-field neural-mass representation of cortical regions, which limits their ability to study how the interaction of local (within a few millimeters) and long-range connectivity affects spatio-temporal SWS dynamics.

Here, we developed a large-scale thalamocortical network model based on spiking excitatory and inhibitory neurons in thalamus and cortex, organized in 6 cortical layers and thalamic core and matrix subsystems, with connectivity based on Human Connectome Project (HCP) diffusion-MRI (dMRI) tractography- based connection probabilities and HCP-derived degree of grey-matter myelination (***Rosen and Halgren, 2021***; ***Van Essen et al., 2013***). To test the contribution of specific elements of connectivity to SO properties, we then systematically modified selected elements of the network connectivity: connection density and radius, synaptic delays and strength.

While we inferred connectivity profiles from dMRI data, predicting the strength of synaptic connections is much harder problem, especially considering that the proposed model is still a significant scaling down of the biological brain. Therefore, a substantial effort of this project was to explore the strength of connections to identify the SWS regimes that match those known from the literature and characterized in our data. We found that altering the balance of excitation and inhibition had a significant impact on the synchronization properties of slow waves. While our baseline

model produced unrealistically synchronized (see below) global slow-waves, reducing the strength of "long-range" excitatory connectivity resulted in models with mixed global and local slow waves, similar to results reported in vivo (***Nir et al., 2011***; ***Funk et al., 2016***). This occurred in models where connections longer than 5-10 mm were reduced four- to five-fold compared to the baseline model, to mimic the high density and strength of local connections in vivo (***Hawkins and Ahmad, 2016***; ***London and Segev, 2001***). Interestingly, this aligns with the results presented by (***Destexhe et al., 1999***), which show an approximately 7mm radius within which slow waves are highly synchronous. Furthermore, (***Riedner et al., 2007***) and (***Vyazovskiy et al., 2007***) have reported that the occurrence of multi-peak slow waves, where each peak has a different origin, increases over the course of sleep, which was proposed to result from a gradual net decrease in the strength of cortico-cortical connections (***Vyazovskiy et al., 2009***) (however, see (***Timofeev and Chauvette, 2017***)). Human recordings (***Siclari et al., 2014***; ***Bernardi et al., 2018***) reported two types of slow waves: Type I - global and more frequently occurring earlier in sleep, and Type II - local slow waves found later in sleep. A recent study suggests that global slow waves (referred to as SO) are responsible for the consolidation of new memories, while local events (referred to as delta oscillations) lead to forgetting (***Kim et al., 2019***).

To validate the model, we compared models with different synaptic connectivity profiles to human recordings during NREM sleep. This was done via a coherence analysis to determine correspondence of signals across distance and frequency. We found the experimental data to closely match the mixed state models, i.e., models showing coexistence of local and global slow-waves. Importantly changing synaptic connectivity in these models led to the models with only local or global slow-waves, still with coherence landscapes closely matching in vivo data. For example, varying the strength of connections greater than 10 mm led to global (3-fold reduction compare to baseline), mixed (4 or 5-fold reduction) and local (6-fold reduction) state models, all closely approximating the experimental data. Interestingly, a 25% increase in all excitatory connections within the mixed-state model triggered a transition to exclusively local slow waves, while a 25% decrease led to global slow oscillations. This suggests that the balance between short- and long-range connections is crucial for maintaining specific slow-wave dynamics and that there is a higher sensitivity to local connectivity. Thus, a 25% increase in all connections increased local excitability enough to generate numerous local slow waves, but a corresponding 25% increase in long-range connectivity was insufficient to organize them into global slow waves.

Taking into account the more frequent occurrence of global slow waves earlier in sleep (***Vyazovskiy et al., 2009***), our model predicts that cortical synapses may exhibit overall potentiation during sleep, in agreement with the hypothesis proposed in (***Timofeev and Chauvette, 2017***). However, a more extensive analysis of synaptic connectivity in the model and analysis of in vivo data are needed to confirm this prediction.

Several studies have revealed a link between long-range intracortical connectivity and the properties of sleep slow waves. In (***Kurth et al., 2017***), it was shown that sleep slow oscillations propagate over longer distances with increasing age, and cortical SO propagation was positively correlated with intrahemispheric myelin content. Additionally, it was found that human subjects with a steeper rising slope of the slow wave exhibited higher axial diffusivity in the temporal fascicle and frontally located white matter tracts (***Piantoni et al., 2013***). These findings suggest that the profiles of sleep oscillations reflect not only the synaptic-level dynamics of the neuronal network but also the microstructural properties of its structural foundation, the white matter tracts. Factors such as normal aging (***Tomasi and Volkow, 2012***) and Alzheimer's Disease (AD) (***Liu et al., 2014***) impact long-range connectivity. Specifically, in patients with severe AD, functional connectivity was notably reduced between regions separated by greater distances, and this loss of long-distance connectivity was associated with a less efficient global and nodal network topology (***Liu et al., 2014***). Alongside well-documented observations of reduced slow wave density in aging (***Mander et al., 2013***) and AD (***Katsuki et al., 2022***), these findings align with our model predictions about the critical role of balancing local and long-range connectivity for maintaining characteristic slow-wave dynamics.

Although our model design achieves high computational efficiency considering the size and complexity of the network, the number of model parameters and simulation time do not currently allow a systematic fitting of the model output to electrophysiological brain signals, as it has been done with smaller computational models (***Cakan et al., 2022***). Nevertheless, the use of realistic parameters for individual neuron dynamics in wake and sleep stages (***Bazhenov et al., 2002***; ***Krishnan et al., 2016***) as well as experimentally grounded cortical connectivity (***Rosen and Halgren, 2021***) allowed us to reproduce the essential characteristics of activity in awake and SWS brain states. Our model allows us to reproduce and to study biologically realistic whole-brain sleep dynamics, and still provides access to the cellular level resolution to study contribution of individual cell and local circuit properties.

In summary, we present a whole-hemisphere thalamocortical network model constrained by realistic local and long range connectivity based on human dMRI data and implementing effects of neuromodulators to account for sleep-wake transitions. The model displays both a biologically realistic awake state with characteristic random neuron firing as well as Type I and Type II slow wave sleep dynamics. Comparing model to empirical data allowed to narrow the connectivity strength profiles while revealing the critical role of such connectivity in generating complex mixed (local/global slow-waves) states, as observed in vivo. Importantly, the model provides both the scale and the level of details required to investigate how large-scale sleep dynamics arise from cellular and circuit level activity.

Methods

Model neurons

Map-based cortical neurons

The model has 10,242 cortical columns uniformly positioned across the surface of one hemisphere, one for each vertex in the ico5 cortical reconstruction reported in ***Rosen et al.*** (***2019***). The medial wall includes 870 of these vertices, so all analyses for this one-hemisphere model were done on the remaining 9372 columns. Each column has 6 cortical layers (L2, L3, L4, L5a, L5b and L6). For each layer in each column, one excitatory (PY) and one inhibitory (IN) neuron were simulated using a phenomenological model based on difference equations ("map-based" model). As shown in our previous work, map-based models use a large discrete time step compared to the small integration time step used by pure conductance-based models while still capturing the dynamics of these models, which enables the simulation of large-scale network dynamics with emergent oscillatory activity (***Rulkov et al., 2004***) including cortical slow waves (***Komarov et al., 2018***).

The activity of pyramidal PY cells was described in terms of four continuous variables sampled at discrete moments of time n : x_n, dictating the trans-membrane potential $V_n = 50x_n - 15$; y_n, representing slow ion channel dynamics; u_n, describing slow hyperpolarizing currents; and k_n, determining the neuron sensitivity to inputs. The activity of IN cells, which biologically have faster spiking dynamics, was modeled using only variable x_n and fixing the other variables to constant values. Dynamical PY variables evolve according to the following system of difference equations, where $n = 1, 2, \ldots$ indexes time steps of 0.5ms in size:

$$\text{spike generation} \begin{cases} x_{n+1} = f_{\text{PY}}(x_n, y_n + \beta_x I_{total}(x_n, u_n), k_n) \\ y_{n+1} = y_n - \mu_1 \cdot (x_n + 1) + \mu_2 \cdot (\sigma p_L + \beta_y I_{total}(x_n, u_n)), \end{cases} \tag{1}$$

$$\text{adaptation} \left[u_{n+1} = \gamma \cdot (u_n + \delta) \right. \tag{2}$$

$$\text{sensitivity to input} \left[k_{n+1} = k_n + H(x_n + 0.5) \cdot (K_1 - k_n) + H(-(x_n + 1)) \cdot (K_0 - k_n)) \right. \tag{3}$$

where function $H(w)$ denotes the Heaviside step function, which takes the value 0 for $w \leq 0$ and 1

otherwise. The reduced model for IN cells is given by

$$x_{n+1} = f_{\text{IN}}\left(x_n, y^* + \psi(\beta_x I_{syn})\right) \tag{4}$$

$$\psi(w) = \begin{cases} -1 & , \ w < -1 \\ w & , \ -1 \leq w \leq 1 \\ 1 & , \ 1 < w \end{cases} \tag{5}$$

where y^* is a fixed value of y_n. We describe each of the system's components below. The model's parameters and their values are summarized in ***Table 2***.

Spike-generating Systems (1) and (4): The nonlinear function f_{PY}, modified by ***Komarov et al.*** (***2018***) from ***Rulkov*** (***2002***), determines the spike waveform as

$$f_{\text{PY}}(x_n, w, k_n) = \begin{cases} \dfrac{\alpha}{1 - x_n} + w & , \ x_n < -0.5 \ \wedge \ w < w_0, \\ \dfrac{\alpha}{1 - x_n} + w_0 + (w - w_0)k_n & , \ x_n < -0.5 \ \wedge \ w \geq w_0, \\ 1 & , \ -0.5 \leq x_n < 1, \\ -1 & , \ x \geq 1 \end{cases} \tag{6}$$

where α and w_0 are constant parameters that control the non-linearity of the spike-generating mechanism. Parameters $\mu_1, \mu_2 < 1$ modulate the slower updating of variable y with respect to variable x, and parameter σ dictates the neuron resting potential as $(1 - \sigma)$. The scaling constants β_x, β_y modulate the input current I_{total} for variables x and y, respectively. The neuron's membrane potential is calculated as $V_n = 50x_n - 15$ and a spike is generated if and only if $V_n > 0.1$. In simulations, the quantity $\beta_x I_{total}(x_n, u_n)$ was manually prevented from reaching 0 by imposing a lower bound of 10^{-4}.

For inhibitory neurons IN, function f_{IN} in (4) is given by

$$f_{\text{IN}}(x_n, w) = \begin{cases} \dfrac{\alpha}{1 - x_n} + w & , \ x_n \leq 0, \\ \alpha + w & , \ 0 < x_n \leq \alpha + w \ \wedge \ x_{n-1} \leq 0, \\ -1 & , \ \text{otherwise} \end{cases} \tag{7}$$

A spike is generated if and only if $0 < x_n \leq \alpha + y^* + \psi(\beta_x I_{syn}) \ \wedge \ x_{n-1} \leq 0$.

Adaptation Equation (2): The slow dynamical variable u_n models the effects of slow hyperpolarizing currents. It integrates the contribution of spikes and exponentially decays towards zero at a rate $\gamma \in (0, 1)$. The value of γ is taken as 0.99 for $x_n < -1$ and 0.995 otherwise. Parameter $\delta = 0.24$ has an effect only if $-0.5 < x_n < 1$; we assume $\delta = 0$ for other values of x_n.

Sensitivity Equation (3): the variable k_n reduces neuron sensitivity to inputs during Up states (i.e. high spiking activity). It adopts the value K_0 (low sensitivity) when voltage x_n crosses threshold -0.5 (i.e. Up state) and switches to $K_1 > K_0$ (high sensitivity) when $x_n < -1$ (i.e. cell leaves Up state). This prevents over-excitation and provides a physiological firing frequency (***Komarov et al., 2018***).

Computation of currents: The total current I_{total} is a sum of external applied dc current (I_{DC}), synaptic inputs (I_{syn}), persistent Na^+ current (I_{Nap}), slow hyperpolarizing currents (I_D), and leak currents (I_{leak}):

$$I_{total} = I_{\text{DC}} + I_{syn} + I_{Nap} + I_D + I_{leak} \tag{8}$$

with the last three dictated primarily by p_{Nap} (maximal conductance of persistent Na^+ current), p_D

and p_L (strength of leak current), respectively.

$$I_{Nap} = \frac{p_{Nap}}{1 + \exp\left(-20(x_n + 0.99)\right)} \tag{9}$$

$$I_D = -p_D u_n(x_n + 1.2) \tag{10}$$

$$I_{leak} = -p_L(x_n - \underbrace{(\sigma p_L - 1)}_{\text{baseline potential}}) \tag{11}$$

For each neuron i, the synaptic current I^i_{syn} is the sum of individual AMPA, GABA$_A$ and NMDA synaptic currents. The individual synaptic current of type X from neuron j to neuron i has the general form

$$g^{ij}_X(n)\left(V_X - V^i_n\right)$$

for AMPA and GABA synapses, and

$$g^{ij}_X(n)\varphi_n\left(V_X - V^i_n\right)$$

for NMDA synapses, with an additional modulator φ_n,

$$\varphi_n = \left(1 + e^{-\frac{V^i_n + 25}{12.5}}\right)^{-1}.$$

Here $g^{ij}_X(n)$ represents conductance at time n for directed connections from neuron j to neuron i. Dynamic synaptic conductances were described by the first-order activation schemes:

$$g^{ij}_X(n+1) = \underbrace{\gamma_{g_X} g^{ij}_X(n)}_{\text{decay}} + \underbrace{d^{ij}_X(n)\frac{G^{syn}_X}{m^i_X} H\left(V^j_n - V_\theta\right)}_{\text{activity-dependent depression}} + \underbrace{\frac{G^{mini}_X}{m^i_X}\eta^{mini}_n(\mu_X)}_{\text{miniature postsynaptic potentials}} \tag{12}$$

with $d(n)$ governed by

$$d^{ij}_X(n+1) = \begin{cases} \gamma^{dep}_{d_x} d^{ij}_X(n) & , V^j_n > V_\theta \ (j \text{ spikes}) \\ 1 + \gamma^{rec}_{d_x}(d^{ij}_X(n) - 1) & , \text{otherwise} \end{cases} \tag{13}$$

for AMPA and GABA$_A$ and

$$d^{ij}_X(n+1) = \begin{cases} d^{ij}_X(n) & , V^j_n > V_\theta (j \text{ spikes}) \\ 1 - (1 - \gamma^{rec}_{d_X})\left(1 - d^{ij}_X(n)\right) & , \text{otherwise} \end{cases} \tag{14}$$

for NMDA type synapses. Here, γ_{g_X} determines the decay rate of synaptic conductance and G^{syn}_X regulates the overall synaptic strength. To keep total synaptic input per cell constant, coefficients G^{syn}_X and G^{mini}_X are scaled by the number m^i_X of synapses of type X incoming to neuron i. The depression variable d_X is dependent on whether the pre-synaptic neuron j spikes at time n or not, that is, if the voltage of neuron j surpasses a threshold V_θ. Lastly, miniature post-synaptic potentials are only present in AMPA and GABA synapses. Variable η^{mini}_n is a spontaneous event from a random Poisson process with mean frequency μ_X, and G^{mini}_X is the constant by which conductance increases in an event ($\eta^{mini}_X = 1$), which produces miniature post-synaptic potentials ("minis") in neuron i (***Stevens, 1993***). Following ***Bazhenov et al.*** (***2002***), the frequency μ_X is modulated in time to account for the reduction in mini frequency after Upstates (***Timofeev et al., 2000***), so that

$$\mu_X = \bar{\mu}_X\left(0.2 + \frac{0.8}{1 + e^{-0.1(n - n^j_0 - 350)}}\right)$$

where n^j_0 is the time of the most recent pre-synaptic spike. This modulation reduces the mini rate to 20% of its maximal value $\bar{\mu}_X$ after a pre-synaptic spike, and then allows recovery to $\bar{\mu}_X$ with time.

Name	Description	PY value	IN value
β_x	x_n input current scaling	0.133	0.05
α	spike nonlinearity parameter	3.65	3.8
w_0	spike nonlinearity parameter	-2.819	-
y^*	fixed y_n value for IN neurons	-	-2.93
μ_1	y_n timescale relative to x_n	0.0008	-
μ_2	y_n timescale relative to x_n	0.002	-
σ	determines neuron resting potential	-0.4	-
β_y	y_n input current scaling	1	-
γ	strength of adaptation	0.99/0.995	-
δ	adaptation parameter	0.24/0	-
K_1	high sensitivity value	0.25	-
K_0	low sensitivity value	0.0025	-
p_{Nap}	persistent Na^+ current strength	0.15	-
p_D	slow hyperpolarizing current strength	4	-
p_L	leak current strength	0.5	-
γ_{g_X}	decay rate of AMPA/GABA$_A$ synaptic conductance	0.995	-
G^{syn}_{AMPA}	AMPA synaptic strength	$7.3 \cdot 10^{-5}$	$2.3 \cdot 10^{-4}$
G^{syn}_{GABA}	GABA$_A$ synaptic strength	$5 \cdot 10^{-5}$	-
G^{syn}_{NMDA}	NMDA synaptic strength	$6.7 \cdot 10^{-10}$	-
G^{mini}_{AMPA}	mini strength for AMPA synapses	$1.6 \cdot 10^{-6}$	
G^{mini}_{GABA}	mini strength for GABA$_A$ synapses	-	0
$\bar{\mu}_X$	mini frequency for AMPA/GABA$_A$ synapses	500	
$\gamma^{dep}_{d_X}$	time scale of synaptic depression	0.05	-
$\gamma^{rec}_{d_X}$	time scale of synaptic recovery	0.005	-
$\gamma^{rec}_{d_{\text{NMDA}}}$	time scale of NMDA synaptic recovery	$5 \cdot 10^{-5}$	-
V_{AMPA}	reversal potential for AMPA synapses	0	-
V_{GABA}	reversal potential for GABA$_A$ synapses	-70	-
V_{NMDA}	reversal potential for NMDA synapses	0	-

Table 2. Map-based model parameter definitions and values. Parameters γ and δ may take one of the two values shown (see text). Sub-index X stands for "AMPA" or "GABA". For all parameters regarding synapses, the PY and IN columns denote the post-synaptic neuron

Name	Description	TC value	RE value	Units
C_m	membrane capacitance	1		$\mu F/cm^2$
g_L	leakage conductance	0.012	0.015	mS/cm^2
E_L	reversal potential	-70	-77	mV
S	cell area	$1.43 \cdot 10^{-4}$	$2.9 \cdot 10^{-4}$	cm^2

Table 3. Parameter definitions and values for conductance-based model

Parameter	Wake	Sleep
p_L	0.15	0.5
p_D	1.6	4.0
G^{syn}_{AMPA} (PY->PY)	$2 \cdot 10^{-5}$	$7.3 \cdot 10^{-5}$
G^{syn}_{AMPA} (PY->IN)	$6.3 \cdot 10^{-5}$	$2.3 \cdot 10^{-4}$
G^{syn}_{GABA} (IN->PY)	$3 \cdot 10^{-5}$	$5 \cdot 10^{-5}$
g_L (TC)	0.007	0.012
g_L (RE)	0.022	0.015

Table 4. Parameter changes between sleep and wake stages

Hodgkin-Huxley thalamic neurons

The thalamus was modeled using a network of core (specific) and matrix (non-specific) nuclei, each consisting of thalamic relay (TC) and reticular (RE) neurons. We simulated 642 thalamic cells of each of these four types. TC and RE cells were modeled as single compartments with membrane potential V governed by the Hodgkin-Huxley kinetics, so that the total membrane current per unit area is given by

$$I = C_m \frac{dV}{dt} = -g_L(V - E_L) - I_{int} - I_{syn} \ ,$$

where C_m is the membrane capacitance,g_L is the non-specific (mixed Na^+ and Cl^-) leakage conductance , E_L is the reversal potential, I_{int} is a sum of active intrinsic currents, and I_{syn} is a sum of synaptic currents. Parameter values and cell areas for both TC and RE neurons are given in ***Table 3***.

Intrinsic currents for both RE and TC cells included a fast sodium current, I_{Na}, a fast potassium current, I_K, a low-threshold Ca^{2+} current, I_T, and a potassium leak current, $I_{KL} = g_{KL}(V - E_{KL})$. For TC cells, an additional hyperpolarization-activated cation current, I_h, was also included. The expressions and parameter values for each of these currents are given in ***Bazhenov et al.*** (***1998a***, 2002); ***Krishnan et al.*** (***2018***); ***Rosen et al.*** (***2019***).

Synaptic currents were calculated as

$$I_{syn} = g_{syn}[O](V - E_{syn}),$$

where g_{syn} is the maximal conductance, $[O](t)$ is the time-dependent fraction of open channels, and E_{syn} is the reversal potential.

Wake to sleep transition

The transition from wake to slow wave sleep stage was accomplished via tuning of several key parameters. The primary tunable parameters of the map model neurons are p_L and p_D, which control the strength of the potassium leak currents and a slow depolarizing current (similar to a calcium current) as described in Equations (10) and (11). Both of these parameters significantly increased from wake to sleep. We further increased the strength of AMPA and GABA synaptic currents, as well as the dendritic potassium leak current, similar to the changes described in ***Krishnan et al.*** (***2016***) (see ***Table 4***).

Network Structure

Our whole hemisphere computational model has realistic local and long-range cortical connectivity. Connections within the column follow those described in the canonical cortical circuit (***Figure 1***A). Additionally, connections within 0.1 mm are strengthened by a factor of 5 to mimic in-vivo increased strength of proximal synapses (***London and Segev, 2001***; ***Hawkins and Ahmad, 2016***). Inhibition is local: IN cells project only to PY cells in the same layer, with connections only in their own column, 1st and 2nd degree neighbors. The strength of inhibitory synapses is 2 times larger within the local column than outside. Finally, miniature postsynaptic potentials on intracortical AMPA synapses are modeled as a Poisson process (as in ***Krishnan et al.*** (***2018***)).

Thalamocortical (TC) and reticular (RE) neurons are modeled using Hodgkin-Huxley dynamics (***Hodgkin and Huxley, 1952***), with 2 subtypes of each to represent matrix and core neurons. The matrix TC neurons have a 45 mm (and 80 mm) fanout radius to cortical excitatory (and inhibitory) neurons while core TC neurons have 12 mm and 13 mm radii, respectively. Within-thalamic connections have 11 mm radii. There are 642 neurons of each of these 4 types (thalamic matrix, thalamic core, reticular matrix, reticular core).

Hierarchically Guided Laminar Connectivity

Long-range connectivity in the model is primarily based on the cortical parcellation into 180 areas proposed by the Human Connectome Project (HCP)-MMP1.0 atlas (***Van Essen et al., 2013***; ***Glasser et al., 2016***). Each parcel was assigned a hierarchical index inversely proportional to its estimated bulk myelination (***Glasser and Essen, 2011***; ***Burt et al., 2018***). Excitatory cortical connections (PY-PY) were then split into 6 classes according to the pre- and post-synaptic hierarchical index: within the local column, within the local parcel (or between contralateral homologs), strongly (>50th percentile) or weakly (≤50th percentile) feedforward (from lower to higher hierarchical index), and strongly or weakly (>, ≤ 50th percentile respectively) feedback (from higher to lower hierarchical index). Based on previous connectivity reports (***Markov et al., 2013***; ***Rockland, 2019***), synaptic weights for these connections were scaled by the factors shown in ***Figure 1*** D.

Diffusion MRI Guided Connection Probability

The connection probability was further scaled based on previous diffusion MRI (dMRI) connectivity studies (***Rosen and Halgren, 2021***). These observations reveal an exponential decay relationship between inter-parcel dMRI connectivity and fiber distance (length constant $\lambda = 23.4$mm, scaling parameter $\beta = 0.17$). In order to obtain a probability of connection at the scale of columns, approximate intercolumnar fiber distances were estimated from geodesic distances. For parcel centroids, intra-hemispheric dMRI streamline distances and their corresponding geodesic distances were found to be related to a first approximation by a linear rational function

$$F(x) = \frac{(p1 * x + p2)}{(x + q1)},$$

with $p1 = 295.6, p2 = -2256$, and $q1 = 69.4$, where x denotes the geodesic distance. Column-wise fiber distances were estimated by applying this function to intercolumnar geodesic distances. Thus, a distance-dependent probability of connection between columns was obtained by applying the dMRI exponential relation to column-wise fiber distances (***Figure 1*** E). Moreover, the residual parcel-wise dMRI connectivity (not distance related, obtained by regressing out the exponential trend) was added back to intercolumnar connections based on the columns' parcels. This distance-independent connectivity accounts for the functional specialization of each parcel. Lastly, conduction delays were set to be proportional to fiber tract distances, with the longest connection (∼226mm) having an assigned delay of 40ms.

Analysis

Modifying Network Structure

We here attempted to create the most biologically realistic model and connectivity possible. However, there is no ground truth to dictate the absolute strength of connection between two individual neurons. While rules exist in our architecture to modify relative strength based on biological connectivity, the base connection strength to be modified is a completely free (and incredibly important) parameter. We first set the base strength level to be high enough to generate Type I slow waves which quickly synchronize across the entire brain. This makes slow wave property analysis more straightforward and less prone to spatial bias when modifying further network parameters, as is the goal of this paper. Hence, we use this global Type I slow wave model for all subsequent analysis aside from analyzing the effect of connection strength itself.

In the case of modulating connection density and range, the synaptic strengths were scaled up proportionally to the loss of connections to retain sufficient activity levels in the network. This allowed us to isolate the effects of patterns of connection apart from changes in total synaptic input. The ablation of connections in these trials was accomplished by setting synaptic connection strengths to 0, removing all functional connectivity.

Local Field Potentials, Amplitude and Frequency

In Figures 2,5,3, the local field potential (LFP) was obtained as the average voltage of Layer 2 at each timestep scaled by a factor of 20. In Figures 6,4,9, the LFP for each local region was further smoothed using a running mean with 20ms window.

Layer LFPs were used to detect cortical upstates. A peak detection algorithm (MATLAB's islocalmax function) was implemented for this purpose, requiring a minimum peak separation of 500ms and a minimum prominence of half the difference between the maximum and minimum values of the signal. The amplitude of each upstate was defined as the difference between the corresponding peak and the lowest point before the next peak. The inverse of each inter-peak interval was used to approximate the oscillation frequency. Average amplitudes and frequencies across all upstates of a simulation are reported in the summary plots of Figures 5,3,7, 8.

Onset/offset Detection

In order to characterize how SO spread through the cortex, we identified the points in time when each neuron transitions from downstate to upstate (onset) and viceversa (offset). Our upstate detection algorithm follows ***Komarov et al.*** (***2018***), based on ***Volgushev et al.*** (***2011***): we set two thresholds, $V^+ = -65$mV and $V^- = -68$mV (see dashed vertical lines in voltage histogram of ***Figure 2*** B), and label any activity above V^+ as an upstate and any activity below V^- as a downstate. This initial detection was further refined by merging any two upstates (or downstates) that were less than 100ms apart, and then removing any remaining upstate (or downstate) lasting less than 100ms, in a similar approach to ***Volgushev et al.*** (***2011***).

To identify onsets and offsets for a particular global upstate, we considered the time window between consecutive minima of the average voltage signal around that upstate (e.g. see black upward triangles in average voltage signal of ***Figure 2*** B). For each neuron, we found the first time (if any) in this window when it reached an upstate (onset), and then the first time after the onset when it reached a downstate (offset). The minimum onset was then subtracted from all onsets so that the earliest neuron would have an assigned time of 0 and all other would have positive delays, or *latencies*. Similarly, the earliest offset was subtracted from all offsets.

In order to evaluate the synchrony of active and silent states, we constructed aggregated histograms of the onset and offset times across all upstates of each simulation. We used the standard deviation of the histograms as an measure for synchrony, with narrow histograms indicating highly synchronized global upstates.

Latency and participation

Latency maps are shown in ***Figure 2*** F (also ***Figure 4*** F, ***Figure 6*** F and ***Figure 9*** F) for each global upstate, representing the delay for activation of each cell after the earliest onset in that upstate. The 3D representation of latencies allows for a visual identification of the source (or sources) of each global upstate, characterized by clusters of adjacent neurons with near-zero latencies.

The percent of participating columns in each upstate was defined as the number of columns with onset delays greater than or equal to 0 over the total number of columns not belonging to the medial wall. Non-participating columns are shown in white in the latency maps for each upstate. The average percent of active columns per upstate is reported in the summary plots in ***Figure 3***F,***Figure 3***F, ***Figure 7*** and ***Figure 8***C-D.

Speed of propagation

To obtain speed of propagation of each upstate, we first identified columns with onset delays under 10ms to get an approximate area of origin. We then selected the column with minimal sum of (geodesic) distances to all columns with onset delays under 10ms, excluding the medial wall. This column was identified as the origin of the upstate. We considered only an area of 150mm radius around the origin to compute propagation speed, in order to avoid interference from waves originating later in other cortical regions. A linear regression was performed between the onset delays of columns in the area and their distances to the origin. For regressions with an $R^2 > .25$, the speed of propagation was defined as the slope of the regression line. The average propagation speed over all upstates is reported in summary plots. Speed is not reported for simulations in which there is not a linear relation between onset delay and distance from the origin, that is, simulations in which regressions for all upstates yield $R^2 \leq .25$.

Experimental Data

Patients and intracranial recordings

Continuous stereo-electroencephalography telemetry and structural imaging were obtained for 298 patients undergoing pre-resection intracranial monitoring for phamaco-resistant focal epilepsy at University of California, San Diego Medical Center, La Jolla CA, the Cleveland Clinic, Cleveland OH, Oregon Health and Science University Hospital, Portland OR, Massachusetts General Hospital, Boston MA, Brigham and Women's Hospital, Boston MA, the Hospital of the University of Pennsylvania, Philadelphia PA, and The University of Alabama Birmingham Hospital, Birmingham AL. These clinical data are recorded as standard of care and written informed consent, approved by each institution's review board, was obtained from each patient before the data were used for research purposes. Recordings were collected with a Nihon Kohen Neurofax (the Cleveland Clinic), Cadwell Arc (Oregon Health and Science University Hospital), or Natus Quantum amplifier (all other clinical sites) and acquired with a sampling frequency of at least 500 Hz. After preliminary inspection, 27 patients with prior resections, highly abnormal sleep patterns, or whose data were overcontaminated with excessive epileptiform activity or technical artifacts were excluded from analysis. A further 35 patients were excluded from further analysis after channel selection and quality control procedures, described below, resulted in them having with fewer than two clean bipolar channel pairs. After quality control, 236 patients (126 female, 101 male, 9 unknown, 36.5 $\pm$ 13.3 (mean $\pm$ stdev.) years old, 22 unknown age) were included in the final analysis.

Channel localization and inter-channel distance

As part of standard of care, a pre-operative T1-weighted high-resolution structural MRI and intero-operative CT scan were obtained for each patient. SEEG contacts were localized as previouslt described (***Dickey et al., 2022***). Briefly, the post-implant CT volume was co-registered to the pre-implant MR volume in standardized 1mm isotropic FreeSurfer space with the general registration module (***Johnson et al., 2007***) in 3D Slicer (***Fedorov et al., 2012***) and each contact's position was determined by manually marking the contact centroid as visualized in the co-registered CT volume.

Cortical surfaces were reconstructed from the MR volume with the FreeSurfer recon-all pipeline (***Fischl, 2012***). Each transcortical bipolar channel was assigned to the white-gray surface vertex nearest to the midpoint of the adjacent contacts. Spherical folding-based surface registration (***Fischl et al., 1999***) was used to map the individual subjects' bipolar channel vertices to the standardized fsaverage ico7 (***Fischl, 2012***) and 32k_FS_LR grayordinate (***Marcus et al., 2013***) atlases as well as to parcels of the HCP-MMP parcellation (***Glasser et al., 2016***). The HCP-MMP parcel assignments of each channel were used to determine the approximate white matter fiber length of the connection between them, using the mean values for a cohort of 1,065 healthy subjects we have previously reported (***Rosen and Halgren, 2021***).

Telemetry preprocessing and channel selection

For each patient, an average of 185.3 $\pm$ 112.0 hours of raw telemetry were analyzed. Data were anti-aliased filtered at 250 Hz and resampled to 500 Hz. To remove line noise, a notch filter was applied at 60, 120, 180, and 240 Hz. On each electrode shaft, data were re-referenced to a bipolar scheme by taking the difference of potentials in adjacent contacts, yielding 30,769 total channels. To ensure that bipolar channels were independent, contact pairs were selected such that no two pairs shared a contact, eliminating just under half of all channels from further consideration. Peaks in the delta band (0.5-2 Hz) signal during high-delta periods were identified and the peri-delta-peak high-gamma band (70-190 Hz) envelope obtained. Transcortical contact pairs were identified by (1) having a midpoint close to the gray-matter–white-matter interface (<5 mm), (2) having a high anticorrelation between the delta-band amplitude and the high gamma band (70-190 Hz) envelope during delta-band peaks, indicative of non-pathological downstates with a surface-negative LFP deflection that quieted spiking, and (3) having high delta-band amplitude with and average delta peak of at least 40 μV, indicative of robust inversion in adjacent contacts. Only contacts with 5 mm pitch were analyzed to standardize absolute bipolar amplitudes and contact pairs located deep in the white matter or in subcortical gray matter were excluded from analysis. All channels were visually inspected to ensure they contained broadly normal non-pathological waveforms such as pathological delta activity. This procedure yielded 4,903 candidate channels which underwent NREM scoring, described below, yielding 9.2 $\pm$ 7.8 hours of putatively clean scored NREM sleep. After scoring, which excluded continuous periods of artifactual or pathological signals, remaining epileptogenic activity was detected with spike template convolution and gross artifacts, with amplitudes > 300 μV. Channels which contained persistent automatically detected interictal spikes or gross artifacts were removed from further analysis, yielding 3,665 channels. Periods containing interictal spikes or gross artifacts in any channel were excluded from analysis in all channels. Finally, after cross-spectral matrices were obtained for each subject as described below, channels with autospectral power more than 3 standard deviations above the pooled channelwise mean in any examined frequency were excluded, leaving 3,588 channels and 37,123 within-patient bivariate channel pairs in the final analysis.

NREM selection

Clean periods of sleep were first manually classified based on ultradian delta power. Within manually identified nightly periods of sleep, NREM sleep was automatically identified by the presences of slow oscillations (SOs) in a manner derived from standard clinical procedures (***Iber et al., 2007***). The density of SOs was ascertained in each 30-second frame and NREM marked for the frame if at least 35% of the frame contained SOs in at least one bipolar channel. The reduction in the number of channels and increase in the percent of frame threshold relative to the clinical standard of 20% of the frame across scalp channels was to accommodate the increased spatial heterogeneity of sleep graphoelements observed intracranially, relative to the scalp (***Mak-McCully et al., 2017***). For this purpose, slow waves were automatically detected with the method described in (***Mak-McCully et al., 2017***), briefly, consecutive delta-band zero-crossings occurring within 0.23-3 s were detected and the top 20% of peaks were retained as SOs. Only periods without detected interictal spikes or

gross artifacts in any bipolar channel were included in subsequent analysis.

Coherence Analysis

Mock Experimental Data

Coherence analysis was performed on both experimental and model data in an identical manner following preprocessing. The model data was preprocessed by averaging the voltages from all cells belonging to each of the 180 parcels (all 6 layers, both excitatory and inhibitory) to mimic what would be recorded by an SEEG electrode. Additionally, white gaussian noise was added to each of the 180 parcel averaged signals. This was done to mimic experimental noise picked up from both other non-neural bodily signals (i.e., muscle movements) and noise from the recording electrode itself. ***Ball et al.*** (***2009***) demonstrated that ECOG arrays show an SNR ranging from 2.22 to 4.37 in relation to eye blink movement artifacts. ***Suarez-Perez et al.*** (***2018***) further calculated the SNR of slow wave sleep upstates (signal) v.s. downstates (noise); they found low frequencies (less than 30 Hz) to have a steady SNR of 4-9, depending on the type of electrode used. At higher frequencies, the SNR dropped severely. With these studies in mind, we implemented an SNR of 5 to account for both body and electrode noise that our model data lacks. The coherence analysis was also run on signals with no noise added - these results can be seen in Figure S5

Signal processing and epoch sampling

A frequency resolved map of each patient's (or simulation's) neural covariability was achieved by estimating the complex cross-spectral matrix among bipolar SEEG channels (for empirical data) or model parcel averages. Narrow-band signals were extracted with a series of second-order resonator filters (matlab's iirpeak) with peaks and 3 dB attenuation bandwidths shown in Table 5. For each frequency the complex analytic signal was extracted via the Hilbert transform. Calculating the variance-covariance matrix of analytic signals yields the cross-spectral matrix. Cross-spectral matrices were normalized into magnitude-squared coherence by squaring the complex modulus of each cross-pairwise cross-spectrum and dividing by the product of the constituent autospectra.

For experimental data, an adaptive procedure was used to obtain stable representative estimates of spontaneous covariability for each patient. Continuous minutes of telemetry were iteratively sampled at random, without replacement, from artifact-free NREM sleep. Sampled minutes of telemetry were appended and prepended with 1.5 seconds of data for filtering and analytic signal extraction. These data were removed prior to covariance estimation to avoid edge artifacts. For each frequency, the coherence matrices were obtained as described above for the incoming minute, ${}_{n+1}\Sigma_{n+1}$, the cumulatively sampled telemetry, ${}_{1}\Sigma_{n+1}$, and, for the second sampled minute onward, the prior cumulatively sampled telemetry, ${}_{1}\Sigma_{n}$. The correlation matrix distance (CMD) (***Herdin et al., 2005***), was calculated between ${}_{1}\Sigma_{n}$ and ${}_{1}\Sigma_{n+1}$, and between ${}_{1}\Sigma_{n}$ and ${}_{n+1}\Sigma_{n+1}$. Starting with the third sampled minute, incoming minutes were rejected if the CMD between ${}_{1}\Sigma_{n}$ and ${}_{n+1}\Sigma_{n+1}$, was more than 3 standard deviations greater than average CMD between ${}_{1}\Sigma_{n}$ and ${}_{n+1}\Sigma_{n+1}$ for all previously sampled minutes. The coherence matrix was considered to have converged when the CMD between ${}_{1}\Sigma_{n}$ and ${}_{1}\Sigma_{n+1}$ was less than 1×10^{-5} and the cumulative cross-spectral matrix was then retained. To dilute the influence of the first sampled minute, this procedure was repeated ten times, and the mean of the resulting cross-spectral matrices was used for subsequent analyses.

Statistical analyses and model fitting

The effect of inter-parcel fiber distance on coherence was assessed by fitting a linear mixed-effects model: log(coherence) distance + 1 + (1 | patient), which accounted for the fixed effects of the predictor variable distance and an intercept term, as well the random effect intercept term grouped by individual (this term was excluded for simulated data). Because of the natural log transformation of the response variable coherence, the linear model is equivalent to an exponential model for the untransformed distance predictor. Therefore, we report the modeled slopes and intercepts as

Frequency (Hz)	Bandwidth (Hz)
0.5	0.5
1	0.5
1.5	0.5
2	0.5
2.5	0.5
3	0.5
3.5	0.5
4	0.5
4.5	0.5
5	0.5
6	1
7	1
8	1
9	1
10	1
12	2
14	2
16	2
18	2
20	2
22	2
24	2
26	2
30	2
35	5
40	5
50	10
60	10
70	10
80	10
90	10
100	10

Table 5. Peaks and 3 dB attenuation bandwidths for the second-order resonator filters used to extract narrow-band signals.

length constants (λ) and scaling terms (α, maximum coherence), respectively. Separate fits were made for each narrowband frequency. Because the parameters of the exponential trend appeared to change at distances greater that 100 mm in experimental, especially for higher frequencies, separate models were fit to electrode pairs 0-100 mm distant, >100 mm, as well as to all pairs. Despite having twice as many parameters, the two-domain model was favored over the one-domain model by both Bayesian and Akaike information criteria for all frequencies and behavioral states. Only the 0-100 mm model parameters are reported here for both experimental and simulation data. All mixed effects linear models were fitted with matlab's fitlme. To avoid the inherent skewness coherence coefficient distributions, coherence values were transformed into z-statistics (***Fisher, 1921***) before model fitting or averaging for display then reverted into coherence coefficients after model fitting or averaging.

Finally, we take the 0.5 Hz lambda and the mean <2 Hz alpha values to describe the key rate of decrease and max coherence in the slow wave range as the primary characteristics of each coherence landscape to be compared across experimental and model data (***Figure 11***).

Acknowledgments

This research was supported by the National Science Foundation Graduate Research Fellowship Program under Grant No. DGE-2038238, and the NIH (grants 1R01MH117155, 1R01NS109553, 1R01MH125557). Data were provided [in part] by the Human Connectome Project, WU-Minn Consortium (Principal Investigators: David Van Essen and Kamil Ugurbil; 1U54MH091657) funded by the 16 NIH Institutes and Centers that support the NIH Blueprint for Neuroscience Research; and by the McDonnell Center for Systems Neuroscience at Washington University.

References

Ball T, Kern M, Mutschler I, Aertsen A, Schulze-Bonhage A. Signal quality of simultaneously recorded invasive and non-invasive EEG. NeuroImage. 2009 Jul; 46(3):708–716. https://linkinghub.elsevier.com/retrieve/pii/S1053811909001827, doi: 10.1016/j.neuroimage.2009.02.028.

Bazhenov M, Timofeev I, Steriade M, Sejnowski TJ. Cellular and Network Models for Intrathalamic Augmenting Responses During 10-Hz Stimulation. Journal of Neurophysiology. 1998 May; 79(5):2730–2748. https://journals.physiology.org/doi/full/10.1152/jn.1998.79.5.2730, doi: 10.1152/jn.1998.79.5.2730, publisher: American Physiological Society.

Bazhenov M, Timofeev I, Steriade M, Sejnowski TJ. Computational Models of Thalamocortical Augmenting Responses. Journal of Neuroscience. 1998 Aug; 18(16):6444–6465. https://www.jneurosci.org/content/18/16/6444, doi: 10.1523/JNEUROSCI.18-16-06444.1998, publisher: Society for Neuroscience Section: ARTICLE.

Bazhenov M, Timofeev I, Steriade M, Sejnowski TJ. Model of Thalamocortical Slow-Wave Sleep Oscillations and Transitions to Activated States. The Journal of Neuroscience. 2002 Oct; 22(19):8691–8704. https://www.jneurosci.org/lookup/doi/10.1523/JNEUROSCI.22-19-08691.2002, doi: 10.1523/JNEUROSCI.22-19-08691.2002.

Bernardi G, Siclari F, Handjaras G, Riedner BA, Tononi G. Local and Widespread Slow Waves in Stable NREM Sleep: Evidence for Distinct Regulation Mechanisms. Frontiers in Human Neuroscience. 2018; 12. https://www.frontiersin.org/articles/10.3389/fnhum.2018.00248.

Bonjean M, Baker T, Lemieux M, Timofeev I, Sejnowski T, Bazhenov M. Corticothalamic Feedback Controls Sleep Spindle Duration In Vivo. Journal of Neuroscience. 2011 Jun; 31(25):9124–9134. https://www.jneurosci.org/lookup/doi/10.1523/JNEUROSCI.0077-11.2011, doi: 10.1523/JNEUROSCI.0077-11.2011.

Bonjean M, Baker T, Bazhenov M, Cash S, Halgren E, Sejnowski T. Interactions between Core and Matrix Thalamocortical Projections in Human Sleep Spindle Synchronization. The Journal of Neuroscience. 2012 Apr; 32(15):5250–5263. https://www.jneurosci.org/lookup/doi/10.1523/JNEUROSCI.6141-11.2012, doi: 10.1523/JNEUROSCI.6141-11.2012.

Burt JB, Demirtaş M, Eckner WJ, Navejar NM, Ji JL, Martin WJ, Bernacchia A, Anticevic A, Murray JD. Hierarchy of transcriptomic specialization across human cortex captured by structural neuroimaging topography. Nature Neuroscience. 2018 Sep; 21(9):1251–1259. doi: 10.1038/s41593-018-0195-0.

Cakan C, Dimulescu C, Khakimova L, Obst D, Flöel A, Obermayer K. Spatiotemporal Patterns of Adaptation-Induced Slow Oscillations in a Whole-Brain Model of Slow-Wave Sleep. Frontiers in Computational Neuroscience. 2022; 15. https://www.frontiersin.org/articles/10.3389/fncom.2021.800101.

Campbell SS, Tobler I. Animal sleep: A review of sleep duration across phylogeny. Neuroscience & Biobehavioral Reviews. 1984 Sep; 8(3):269–300. https://linkinghub.elsevier.com/retrieve/pii/014976348490054X, doi: 10.1016/0149-7634(84)90054-X.

Compte A, Sanchez-Vives MV, McCormick DA, Wang XJ. Cellular and Network Mechanisms of Slow Oscillatory Activity (<1 Hz) and Wave Propagations in a Cortical Network Model. Journal of Neurophysiology. 2003 May; 89(5):2707–2725. https://www.physiology.org/doi/10.1152/jn.00845.2002, doi: 10.1152/jn.00845.2002.

Crunelli V, Hughes SW. The slow (<1 Hz) rhythm of non-REM sleep: a dialogue between three cardinal oscillators. Nature Neuroscience. 2010 Jan; 13(1):9–17. https://www.nature.com/articles/nn.2445, doi: 10.1038/nn.2445, number: 1 Publisher: Nature Publishing Group.

Csercsa R, Dombovári B, Fabó D, Wittner L, Erőss L, Entz L, Sólyom A, Rásonyi G, Szűcs A, Kelemen A, Jakus R, Juhos V, Grand L, Magony A, Halász P, Freund TF, Maglóczky Z, Cash SS, Papp L, Karmos G, et al. Laminar analysis of slow wave activity in humans. Brain. 2010 Sep; 133(9):2814–2829. https://doi.org/10.1093/brain/awq169, doi: 10.1093/brain/awq169.

Destexhe A. Self-sustained asynchronous irregular states and Up-Down states in thalamic, cortical and thalamocortical networks of nonlinear integrate-and-fire neurons. Journal of Computational Neuroscience. 2009 Dec; 27(3):493–506. doi: 10.1007/s10827-009-0164-4.

Destexhe A, Contreras D, Steriade M. Spatiotemporal Analysis of Local Field Potentials and Unit Discharges in Cat Cerebral Cortex during Natural Wake and Sleep States. The Journal of Neuroscience. 1999 Jun; 19(11):4595–4608. https://www.ncbi.nlm.nih.gov/pmc/articles/PMC6782626/, doi: 10.1523/JNEUROSCI.19-11-04595.1999.

Dickey CW, Verzhbinsky IA, Jiang X, Rosen BQ, Kajfez S, Stedelin B, Shih JJ, Ben-Haim S, Raslan AM, Eskandar EN, Gonzalez-Martinez J, Cash SS, Halgren E. Widespread ripples synchronize human cortical activity during sleep, waking, and memory recall. Proceedings of the National Academy of Sciences. 2022 Jul; 119(28):e2107797119. https://pnas.org/doi/full/10.1073/pnas.2107797119, doi: 10.1073/pnas.2107797119.

Donoghue T, Haller M, Peterson EJ, Varma P, Sebastian P, Gao R, Noto T, Lara AH, Wallis JD, Knight RT, Shestyuk A, Voytek B. Parameterizing neural power spectra into periodic and aperiodic components. Nature Neuroscience. 2020 Dec; 23(12):1655–1665. https://www.nature.com/articles/s41593-020-00744-x, doi: 10.1038/s41593-020-00744-x, number: 12 Publisher: Nature Publishing Group.

Engel TA, Steinmetz NA, Gieselmann MA, Thiele A, Moore T, Boahen K. Selective modulation of cortical state during spatial attention. Science. 2016 Dec; 354(6316):1140–1144. https://www.science.org/doi/full/10.1126/science.aag1420, doi: 10.1126/science.aag1420, publisher: American Association for the Advancement of Science.

Eschenko O, Mölle M, Born J, Sara SJ. Elevated Sleep Spindle Density after Learning or after Retrieval in Rats. Journal of Neuroscience. 2006 Dec; 26(50):12914–12920. https://www.jneurosci.org/content/26/50/12914, doi: 10.1523/JNEUROSCI.3175-06.2006, publisher: Society for Neuroscience Section: Articles.

Fedorov A, Beichel R, Kalpathy-Cramer J, Finet J, Fillion-Robin JC, Pujol S, Bauer C, Jennings D, Fennessy F, Sonka M, Buatti J, Aylward S, Miller JV, Pieper S, Kikinis R. 3D Slicer as an image computing platform for the Quantitative Imaging Network. Magnetic Resonance Imaging. 2012 Nov; 30(9):1323–1341. https://linkinghub.elsevier.com/retrieve/pii/S0730725X12001816, doi: 10.1016/j.mri.2012.05.001.

Fischl B. FreeSurfer. Neuroimage. 2012; 62(2):774–781. ISBN: 1053-8119 Publisher: Elsevier.

Fischl B, Sereno MI, Tootell RBH, Dale AM. High-resolution intersubject averaging and a coordinate system for the cortical surface. Human Brain Mapping. 1999; 8(4):272–284. https://onlinelibrary.wiley.com/doi/10.1002/(SICI)1097-0193(1999)8:4<272::AID-HBM10>3.0.CO;2-4, doi: 10.1002/(SICI)1097-0193(1999)8:4<272::AID-HBM10>3.0.CO;2-4.

Fisher RA. On the" Probable Error" of a Coefficient of Correlation Deduced from a Small Sample. Metron. 1921; 1:3–32.

Funk CM, Honjoh S, Rodriguez AV, Cirelli C, Tononi G. Local slow waves in superficial layers of primary cortical areas during REM sleep. Current biology : CB. 2016 Feb; 26(3):396–403. https://www.ncbi.nlm.nih.gov/pmc/articles/PMC4747819/, doi: 10.1016/j.cub.2015.11.062.

Glasser MF, Coalson TS, Robinson EC, Hacker CD, Harwell J, Yacoub E, Ugurbil K, Andersson J, Beckmann CF, Jenkinson M, Smith SM, Van Essen DC. A multi-modal parcellation of human cerebral cortex. Nature. 2016 Aug; 536(7615):171–178. https://www.nature.com/articles/nature18933, doi: 10.1038/nature18933.

Glasser MF, Essen DCV. Mapping Human Cortical Areas In Vivo Based on Myelin Content as Revealed by T1- and T2-Weighted MRI. Journal of Neuroscience. 2011 Aug; 31(32):11597–11616. https://www.jneurosci.org/content/31/32/11597, doi: 10.1523/JNEUROSCI.2180-11.2011, publisher: Society for Neuroscience Section: Articles.

Goldman JS, Kusch L, Aquilue D, Yalçınkaya BH, Depannemaecker D, Ancourt K, Nghiem TAE, Jirsa V, Destexhe A. A comprehensive neural simulation of slow-wave sleep and highly responsive wakefulness dynamics. Frontiers in Computational Neuroscience. 2023 Jan; 16:1058957. https://www.frontiersin.org/articles/10.3389/fncom.2022.1058957/full, doi: 10.3389/fncom.2022.1058957.

Hanlon EC, Faraguna U, Vyazovskiy VV, Tononi G, Cirelli C. Effects of Skilled Training on Sleep Slow Wave Activity and Cortical Gene Expression in the Rat. Sleep. 2009 Jun; 32(6):719–729. https://doi.org/10.1093/sleep/32.6.719, doi: 10.1093/sleep/32.6.719.

Hawkins J, Ahmad S. Why Neurons Have Thousands of Synapses, a Theory of Sequence Memory in Neocortex. Frontiers in Neural Circuits. 2016 Mar; 10:23. https://www.ncbi.nlm.nih.gov/pmc/articles/PMC4811948/, doi: 10.3389/fncir.2016.00023.

Herdin M, Czink N, Ozcelik H, Bonek E. Correlation Matrix Distance, a Meaningful Measure for Evaluation of Non-Stationary MIMO Channels. In: *2005 IEEE 61st Vehicular Technology Conference*, vol. 1 Stockholm, Sweden: IEEE; 2005. p. 136–140. http://ieeexplore.ieee.org/document/1543265/, doi: 10.1109/VETECS.2005.1543265.

Hill S, Tononi G. Modeling Sleep and Wakefulness in the Thalamocortical System. Journal of Neurophysiology. 2005 Mar; 93(3):1671–1698. https://journals.physiology.org/doi/full/10.1152/jn.00915.2004, doi: 10.1152/jn.00915.2004, publisher: American Physiological Society.

Hodgkin AL, Huxley AF. A quantitative description of membrane current and its application to conduction and excitation in nerve. The Journal of Physiology. 1952 Aug; 117(4):500–544. https://www.ncbi.nlm.nih.gov/pmc/articles/PMC1392413/, doi: 10.1113/jphysiol.1952.sp004764, publisher: Wiley-Blackwell.

Huber R, Felice Ghilardi M, Massimini M, Tononi G. Local sleep and learning. Nature. 2004 Jul; 430(6995):78–81. https://www.nature.com/articles/nature02663, doi: 10.1038/nature02663, number: 6995 Publisher: Nature Publishing Group.

Hung CS, Sarasso S, Ferrarelli F, Riedner B, Ghilardi MF, Cirelli C, Tononi G. Local experience-dependent changes in the wake EEG after prolonged wakefulness. Sleep. 2013; 36(1):59–72. https://academic.oup.com/sleep/article-abstract/36/1/59/2656920, publisher: Oxford University Press.

Iber C, Ancoli-Israel S, Chesson A, Quan S. Manual for the Scoring of Sleep and Associated Events: Rules, Terminology and Technical Specifications. American Academy of Sleep Medicine. 2007; 59.

Isomura Y, Sirota A, Özen S, Montgomery S, Mizuseki K, Henze DA, Buzsáki G. Integration and Segregation of Activity in Entorhinal-Hippocampal Subregions by Neocortical Slow Oscillations. Neuron. 2006 Dec; 52(5):871–882. https://linkinghub.elsevier.com/retrieve/pii/S0896627306008221, doi: 10.1016/j.neuron.2006.10.023.

Ji D, Wilson MA. Coordinated memory replay in the visual cortex and hippocampus during sleep. Nature Neuroscience. 2007 Jan; 10(1):100–107. https://www.nature.com/articles/nn1825, doi: 10.1038/nn1825.

Johnson H, Harris G, Williams K. BRAINSFit: mutual information rigid registrations of whole-brain 3D images, using the insight toolkit. Insight J. 2007; 57(1):1–10.

Katsuki F, Gerashchenko D, Brown RE. Alterations of sleep oscillations in Alzheimer's disease: A potential role for GABAergic neurons in the cortex, hippocampus, and thalamus. Brain Research Bulletin. 2022 Sep; 187:181–198. https://linkinghub.elsevier.com/retrieve/pii/S0361923022001654, doi: 10.1016/j.brainresbull.2022.07.002.

van Kempen J, Gieselmann MA, Boyd M, Steinmetz NA, Moore T, Engel TA, Thiele A. Top-down coordination of local cortical state during selective attention. Neuron. 2021; 109(5):894–904. https://www.cell.com/neuron/pdf/S0896-6273(20)30995-8.pdf, publisher: Elsevier.

Kim J, Gulati T, Ganguly K. Competing Roles of Slow Oscillations and Delta Waves in Memory Consolidation versus Forgetting. Cell. 2019 Oct; 179(2):514–526.e13. https://linkinghub.elsevier.com/retrieve/pii/S0092867419309596, doi: 10.1016/j.cell.2019.08.040.

Komarov M, Krishnan G, Chauvette S, Rulkov N, Timofeev I, Bazhenov M. New class of reduced computationally efficient neuronal models for large-scale simulations of brain dynamics. Journal of Computational Neuroscience. 2018 Feb; 44(1):1–24. http://link.springer.com/10.1007/s10827-017-0663-7, doi: 10.1007/s10827-017-0663-7.

Korman M, Doyon J, Doljansky J, Carrier J, Dagan Y, Karni A. Daytime sleep condenses the time course of motor memory consolidation. Nature Neuroscience. 2007 Sep; 10(9):1206–1213. https://www.nature.com/articles/nn1959, doi: 10.1038/nn1959, number: 9 Publisher: Nature Publishing Group.

Krishnan GP, Chauvette S, Shamie I, Soltani S, Timofeev I, Cash SS, Halgren E, Bazhenov M. Cellular and neurochemical basis of sleep stages in the thalamocortical network. eLife. 2016 Nov; 5:e18607. https://elifesciences.org/articles/18607, doi: 10.7554/eLife.18607.

Krishnan GP, Rosen BQ, Chen JY, Muller L, Sejnowski TJ, Cash SS, Halgren E, Bazhenov M. Thalamocortical and intracortical laminar connectivity determines sleep spindle properties. PLOS Computational Biology. 2018 Jun; 14(6):e1006171. https://journals.plos.org/ploscompbiol/article?id=10.1371/journal.pcbi.1006171, doi: 10.1371/journal.pcbi.1006171, publisher: Public Library of Science.

Kurth S, Riedner BA, Dean DC, O'Muircheartaigh J, Huber R, Jenni OG, Deoni SCL, LeBourgeois MK. Traveling Slow Oscillations During Sleep: A Marker of Brain Connectivity in Childhood. Sleep. 2017 Sep; 40(9). https://academic.oup.com/sleep/article/doi/10.1093/sleep/zsx121/3953857, doi: 10.1093/sleep/zsx121.

Lee SH, Dan Y. Neuromodulation of Brain States. Neuron. 2012 Oct; 76(1):209–222. https://linkinghub.elsevier.com/retrieve/pii/S0896627312008203, doi: 10.1016/j.neuron.2012.09.012.

Leung LC, Mourrain P. Sleep: Short Sleepers Should Keep Count of Their Hypocretin Neurons. Current Biology. 2018 May; 28(9):R558–R560. https://linkinghub.elsevier.com/retrieve/pii/S0960982218303075, doi: 10.1016/j.cub.2018.03.006.

Levenstein D, Buzsáki G, Rinzel J. NREM sleep in the rodent neocortex and hippocampus reflects excitable dynamics. Nature Communications. 2019 Jun; 10(1):2478. https://www.nature.com/articles/s41467-019-10327-5, doi: 10.1038/s41467-019-10327-5.

Liu Y, Yu C, Zhang X, Liu J, Duan Y, Alexander-Bloch AF, Liu B, Jiang T, Bullmore E. Impaired Long Distance Functional Connectivity and Weighted Network Architecture in Alzheimer's Disease. Cerebral Cortex. 2014 Jun; 24(6):1422–1435. https://academic.oup.com/cercor/article-lookup/doi/10.1093/cercor/bhs410, doi: 10.1093/cercor/bhs410.

London M, Segev I. Synaptic scaling in vitro and in vivo. Nature Neuroscience. 2001 Sep; 4(9):853–854. https://www.nature.com/articles/nn0901-853, doi: 10.1038/nn0901-853, number: 9 Publisher: Nature Publishing Group.

Mak-McCully RA, Rolland M, Sargsyan A, Gonzalez C, Magnin M, Chauvel P, Rey M, Bastuji H, Halgren E. Coordination of cortical and thalamic activity during non-REM sleep in humans. Nature Communications. 2017 May; 8(1):15499. https://www.nature.com/articles/ncomms15499, doi: 10.1038/ncomms15499.

Mander BA, Rao V, Lu B, Saletin JM, Lindquist JR, Ancoli-Israel S, Jagust W, Walker MP. Prefrontal atrophy, disrupted NREM slow waves and impaired hippocampal-dependent memory in aging. Nature Neuroscience. 2013 Mar; 16(3):357–364. https://www.nature.com/articles/nn.3324, doi: 10.1038/nn.3324.

Marcus DS, Harms MP, Snyder AZ, Jenkinson M, Wilson JA, Glasser MF, Barch DM, Archie KA, Burgess GC, Ramaratnam M, Hodge M, Horton W, Herrick R, Olsen T, McKay M, House M, Hileman M, Reid E, Harwell J, Coalson T, et al. Human Connectome Project informatics: Quality control, database services, and data visualization. NeuroImage. 2013 Oct; 80:202–219. https://linkinghub.elsevier.com/retrieve/pii/S1053811913005776, doi: 10.1016/j.neuroimage.2013.05.077.

Markov NT, Ercsey-Ravasz M, Van Essen DC, Knoblauch K, Toroczkai Z, Kennedy H. Cortical High-Density Counterstream Architectures. Science. 2013 Nov; 342(6158):1238406. https://www.science.org/doi/full/10.1126/science.1238406, doi: 10.1126/science.1238406, publisher: American Association for the Advancement of Science.

Mascetti L, Muto V, Matarazzo L, Foret A, Ziegler E, Albouy G, Sterpenich V, Schmidt C, Degueldre C, Leclercq Y, Phillips C, Luxen A, Vandewalle G, Vogels R, Maquet P, Balteau E. The Impact of Visual Perceptual Learning on Sleep and Local Slow-Wave Initiation. The Journal of Neuroscience. 2013 Feb; 33(8):3323–3331. https://www.ncbi.nlm.nih.gov/pmc/articles/PMC6619511/, doi: 10.1523/JNEUROSCI.0763-12.2013.

Mölle M, Eschenko O, Gais S, Sara SJ, Born J. The influence of learning on sleep slow oscillations and associated spindles and ripples in humans and rats. European Journal of Neuroscience. 2009 Mar; 29(5):1071–1081. https://onlinelibrary.wiley.com/doi/10.1111/j.1460-9568.2009.06654.x, doi: 10.1111/j.1460-9568.2009.06654.x.

Nazari M, Karimi Abadchi J, Naghizadeh M, Bermudez-Contreras EJ, McNaughton BL, Tatsuno M, Mohajerani MH. Regional variation in cholinergic terminal activity determines the non-uniform occurrence of cortical slow waves during REM sleep in mice. Cell Reports. 2023 May; 42(5):112450. https://linkinghub.elsevier.com/retrieve/pii/S2211124723004618, doi: 10.1016/j.celrep.2023.112450.

Nir Y, Staba RJ, Andrillon T, Vyazovskiy VV, Cirelli C, Fried I, Tononi G. Regional slow waves and spindles in human sleep. Neuron. 2011 Apr; 70(1):153–169. doi: 10.1016/j.neuron.2011.02.043.

Nobili L, Ferrara M, Moroni F, De Gennaro L, Russo GL, Campus C, Cardinale F, De Carli F. Dissociated wake-like and sleep-like electro-cortical activity during sleep. NeuroImage. 2011 Sep; 58(2):612–619. https://www.sciencedirect.com/science/article/pii/S1053811911006501, doi: 10.1016/j.neuroimage.2011.06.032.

Peter-Derex L, Magnin M, Bastuji H. Heterogeneity of arousals in human sleep: A stereo-electroencephalographic study. NeuroImage. 2015 Dec; 123:229–244. https://www.sciencedirect.com/science/article/pii/S1053811915006771, doi: 10.1016/j.neuroimage.2015.07.057.

Pfaff D, Ribeiro A, Matthews J, Kow L. *Concepts and Mechanisms of Generalized Central Nervous System Arousal*. Annals of the New York Academy of Sciences. 2008 May; 1129(1):11–25. https://nyaspubs.onlinelibrary.wiley.com/doi/10.1196/annals.1417.019, doi: 10.1196/annals.1417.019.

Piantoni G, Poil SS, Linkenkaer-Hansen K, Verweij IM, Ramautar JR, Van Someren EJW, Van Der Werf YD. Individual Differences in White Matter Diffusion Affect Sleep Oscillations. The Journal of Neuroscience. 2013 Jan; 33(1):227–233. https://www.jneurosci.org/lookup/doi/10.1523/JNEUROSCI.2030-12.2013, doi: 10.1523/JNEUROSCI.2030-12.2013.

Pugin F, Metz AJ, Wolf M, Achermann P, Jenni OG, Huber R. Local increase of sleep slow wave activity after three weeks of working memory training in children and adolescents. Sleep. 2015 Apr; 38(4):607–614. doi: 10.5665/sleep.4580.

Quercia A, Zappasodi F, Committeri G, Ferrara M. Local Use-Dependent Sleep in Wakefulness Links Performance Errors to Learning. Frontiers in Human Neuroscience. 2018; 12. https://www.frontiersin.org/articles/10.3389/fnhum.2018.00122.

Rasch B, Born J. About Sleep's Role in Memory. Physiological Reviews. 2013 Apr; 93(2):681–766. https://journals.physiology.org/doi/full/10.1152/physrev.00032.2012, doi: 10.1152/physrev.00032.2012, publisher: American Physiological Society.

Rasch B, Büchel C, Gais S, Born J. Odor Cues During Slow-Wave Sleep Prompt Declarative Memory Consolidation. Science. 2007 Mar; 315(5817):1426–1429. https://www.science.org/doi/10.1126/science.1138581, doi: 10.1126/science.1138581.

Riedner BA, Vyazovskiy VV, Huber R, Massimini M, Esser S, Murphy M, Tononi G. Sleep Homeostasis and Cortical Synchronization: III. A High-Density EEG Study of Sleep Slow Waves in Humans. Sleep. 2007 Dec; 30(12):1643–1657. https://www.ncbi.nlm.nih.gov/pmc/articles/PMC2276133/.

Rockland KS. What do we know about laminar connectivity? NeuroImage. 2019 Aug; 197:772–784. doi: 10.1016/j.neuroimage.2017.07.032.

Rosanova M, Ulrich D. Pattern-Specific Associative Long-Term Potentiation Induced by a Sleep Spindle-Related Spike Train. The Journal of Neuroscience. 2005 Oct; 25(41):9398–9405. https://www.jneurosci.org/lookup/doi/10.1523/JNEUROSCI.2149-05.2005, doi: 10.1523/JNEUROSCI.2149-05.2005.

Rosen BQ, Krishnan GP, Sanda P, Komarov M, Sejnowski T, Rulkov N, Ulbert I, Eross L, Madsen J, Devinsky O, Doyle W, Fabo D, Cash S, Bazhenov M, Halgren E. Simulating human sleep spindle MEG and EEG from ion channel and circuit level dynamics. Journal of Neuroscience Methods. 2019 Mar; 316:46–57. https://www.sciencedirect.com/science/article/pii/S0165027018303108, doi: 10.1016/j.jneumeth.2018.10.002.

Rosen BQ, Halgren E. A Whole-Cortex Probabilistic Diffusion Tractography Connectome. eneuro. 2021 Jan; 8(1):ENEURO.0416–20.2020. https://www.eneuro.org/lookup/doi/10.1523/ENEURO.0416-20.2020, doi: 10.1523/ENEURO.0416-20.2020.

Rulkov NF, Timofeev I, Bazhenov M. Oscillations in Large-Scale Cortical Networks: Map-Based Model. Journal of Computational Neuroscience. 2004 Sep; 17(2):203–223. http://link.springer.com/10.1023/B:JCNS.0000037683.55688.7e, doi: 10.1023/B:JCNS.0000037683.55688.7e.

Rulkov NF. Modeling of spiking-bursting neural behavior using two-dimensional map. Physical Review E. 2002 Apr; 65(4):041922. https://link.aps.org/doi/10.1103/PhysRevE.65.041922, doi: 10.1103/PhysRevE.65.041922, publisher: American Physical Society.

Shepherd GMG, Yamawaki N. Untangling the cortico-thalamo-cortical loop: cellular pieces of a knotty circuit puzzle. Nature Reviews Neuroscience. 2021 Jul; 22(7):389–406. https://www.nature.com/articles/s41583-021-00459-3, doi: 10.1038/s41583-021-00459-3.

Siclari F, Bernardi G, Riedner BA, LaRocque JJ, Benca RM, Tononi G. Two Distinct Synchronization Processes in the Transition to Sleep: A High-Density Electroencephalographic Study. Sleep. 2014 Oct; 37(10):1621–1637. https://www.ncbi.nlm.nih.gov/pmc/articles/PMC4173919/, doi: 10.5665/sleep.4070.

Siclari F, Tononi G. Local aspects of sleep and wakefulness. Current Opinion in Neurobiology. 2017 Jun; 44:222–227. https://linkinghub.elsevier.com/retrieve/pii/S0959438816302410, doi: 10.1016/j.conb.2017.05.008.

Soltani S, Chauvette S, Bukhtiyarova O, Lina JM, Dubé J, Seigneur J, Carrier J, Timofeev I. Sleep–Wake Cycle in Young and Older Mice. Frontiers in Systems Neuroscience. 2019; 13. https://www.frontiersin.org/articles/10.3389/fnsys.2019.00051.

Steriade M, Nunez A, Amzica F. Intracellular analysis of relations between the slow (<1 Hz) neocortical oscillation and other sleep rhythms of the electroencephalogram. Journal of Neuroscience. 1993 Aug; 13(8):3266–3283. https://www.jneurosci.org/content/13/8/3266, doi: 10.1523/JNEUROSCI.13-08-03266.1993, publisher: Society for Neuroscience Section: Articles.

Steriade M, Timofeev I, Grenier F. Natural Waking and Sleep States: A View From Inside Neocortical Neurons. Journal of Neurophysiology. 2001 May; 85(5):1969–1985. https://journals.physiology.org/doi/full/10.1152/jn.2001.85.5.1969, doi: 10.1152/jn.2001.85.5.1969, publisher: American Physiological Society.

Steriade M, McCormick DA, Sejnowski TJ. Thalamocortical Oscillations in the Sleeping and Aroused Brain. Science. 1993 Oct; 262(5134):679–685. https://www.science.org/doi/10.1126/science.8235588, doi: 10.1126/science.8235588, publisher: American Association for the Advancement of Science.

Steriade MM, McCarley RW. Brainstem Control of Wakefulness and Sleep. Springer Science & Business Media; 2013. Google-Books-ID: X5juBwAAQBAJ.

Stevens CF. Quantal release of neurotransmitter and long-term potentiation. Cell. 1993 Jan; 72:55–63. https://www.sciencedirect.com/science/article/pii/S0092867405800285, doi: 10.1016/S0092-8674(05)80028-5.

Suarez-Perez A, Gabriel G, Rebollo B, Illa X, Guimerà-Brunet A, Hernández-Ferrer J, Martínez MT, Villa R, Sanchez-Vives MV. Quantification of Signal-to-Noise Ratio in Cerebral Cortex Recordings Using Flexible MEAs With Co-localized Platinum Black, Carbon Nanotubes, and Gold Electrodes. Frontiers in Neuroscience. 2018 Nov; 12:862. https://www.frontiersin.org/article/10.3389/fnins.2018.00862/full, doi: 10.3389/fnins.2018.00862.

Timofeev I, Grenier F, Bazhenov M, Sejnowski TJ, Steriade M. Origin of Slow Cortical Oscillations in Deafferented Cortical Slabs. Cerebral Cortex. 2000 Dec; 10(12):1185–1199. https://doi.org/10.1093/cercor/10.12.1185, doi: 10.1093/cercor/10.12.1185.

Timofeev I, Chauvette S. Sleep slow oscillation and plasticity. Current Opinion in Neurobiology. 2017 Jun; 44:116–126. https://www.sciencedirect.com/science/article/pii/S0959438817300417, doi: 10.1016/j.conb.2017.03.019.

Tomasi D, Volkow ND. Aging and functional brain networks. Molecular Psychiatry. 2012 May; 17(5):549–558. https://www.nature.com/articles/mp201181, doi: 10.1038/mp.2011.81.

Van Essen DC, Smith SM, Barch DM, Behrens TEJ, Yacoub E, Ugurbil K. The WU-Minn Human Connectome Project: An overview. NeuroImage. 2013 Oct; 80:62–79. https://www.sciencedirect.com/science/article/pii/S1053811913005351, doi: 10.1016/j.neuroimage.2013.05.041.

Volgushev M, Chauvette S, Timofeev I. Long-range correlation of the membrane potential in neocortical neurons during slow oscillation. In: *Progress in Brain Research*, vol. 193 Elsevier; 2011.p. 181–199. https://linkinghub.elsevier.com/retrieve/pii/B9780444538390000120, doi: 10.1016/B978-0-444-53839-0.00012-0.

Vyazovskiy VV, Olcese U, Hanlon EC, Nir Y, Cirelli C, Tononi G. Local sleep in awake rats. Nature. 2011 Apr; 472(7344):443–447. https://www.ncbi.nlm.nih.gov/pmc/articles/PMC3085007/, doi: 10.1038/nature10009.

Vyazovskiy VV, Olcese U, Lazimy YM, Faraguna U, Esser SK, Williams JC, Cirelli C, Tononi G. Cortical Firing and Sleep Homeostasis. Neuron. 2009 Sep; 63(6):865–878. https://linkinghub.elsevier.com/retrieve/pii/S0896627309006370, doi: 10.1016/j.neuron.2009.08.024.

Vyazovskiy VV, Riedner BA, Cirelli C, Tononi G. Sleep Homeostasis and Cortical Synchronization: II. A Local Field Potential Study of Sleep Slow Waves in the Rat. Sleep. 2007 Dec; 30(12):1631–1642. https://www.ncbi.nlm.nih.gov/pmc/articles/PMC2276140/.

Wierzynski CM, Lubenov EV, Gu M, Siapas AG. State-Dependent Spike-Timing Relationships between Hippocampal and Prefrontal Circuits during Sleep. Neuron. 2009 Feb; 61(4):587–596. https://linkinghub.elsevier.com/retrieve/pii/S0896627309000786, doi: 10.1016/j.neuron.2009.01.011.

Wilckens KA, Ferrarelli F, Walker MP, Buysse DJ. Slow-Wave Activity Enhancement to Improve Cognition. Trends in Neurosciences. 2018 Jul; 41(7):470–482. https://www.cell.com/trends/neurosciences/abstract/S0166-2236(18)30064-X, doi: 10.1016/j.tins.2018.03.003, publisher: Elsevier.

Winkelman JW, Lecea LD. Sleep and neuropsychiatric illness. Neuropsychopharmacology. 2020 Jan; 45(1):1–2. https://www.nature.com/articles/s41386-019-0514-5, doi: 10.1038/s41386-019-0514-5.

Supplementary Information

Activity by Layer and Cell Type

Figure S1 shows the activity of all 6 modeled layers baseline SO simulation in ***Figure 2***. Activity is largely synchronized across layers.

Figure S2 shows the activity of modeled core and matrix thalamocortical (TC, TCa) and reticular (RE, REa) cells as well as inhibitory (IN) cells.

Graph Properties

Figure S3 and ***Figure S4*** show graph properties of the networks for the baseline slow wave simulation in ***Figure 2*** and for the restricted range $R = 2.5mm$ simulation in ***Figure 6***. For the full connectivity network, initiation zones (characterized by low mean onset delay) generally correspond to lower in-degree and out-degree regions. For the local connectivity network, active regions during Upstates in ***Figure 6***F correspond to regions with high in-degree and out-degree.

Model Coherence

Figure S5 shows the coherence analysis results when no noise is added to model data. In this plot, experimental data clusters more closely with purely local slow wave models. However, mixed models are also nearby, and several global models only a little bit farther away. In general, adding noise primarily shifts the alpha values of the simulated models down (lowering peak coherence).

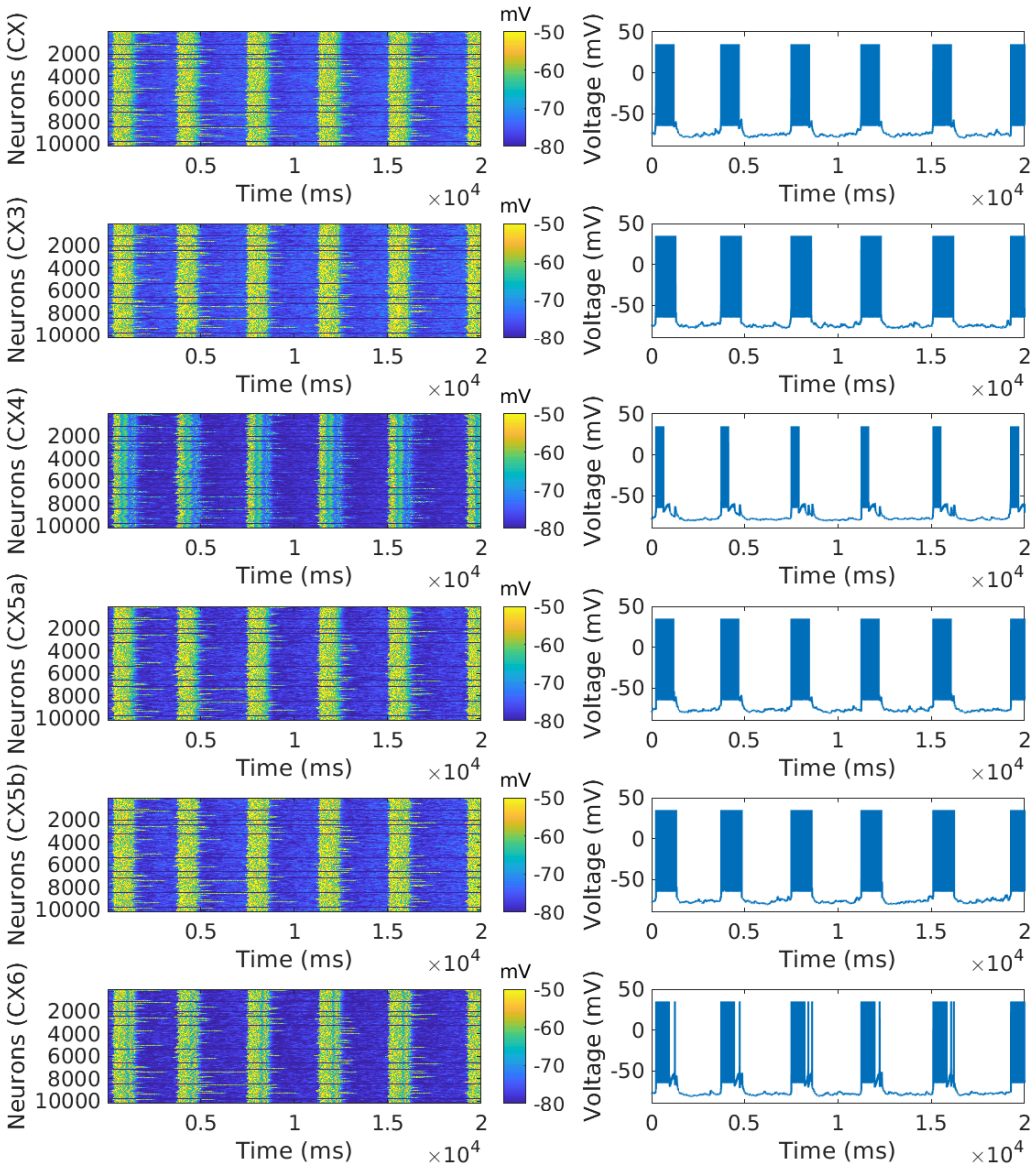

Figure S1. Neuronal activity in all 6 layers during the baseline SO simulation from ***Figure 2***

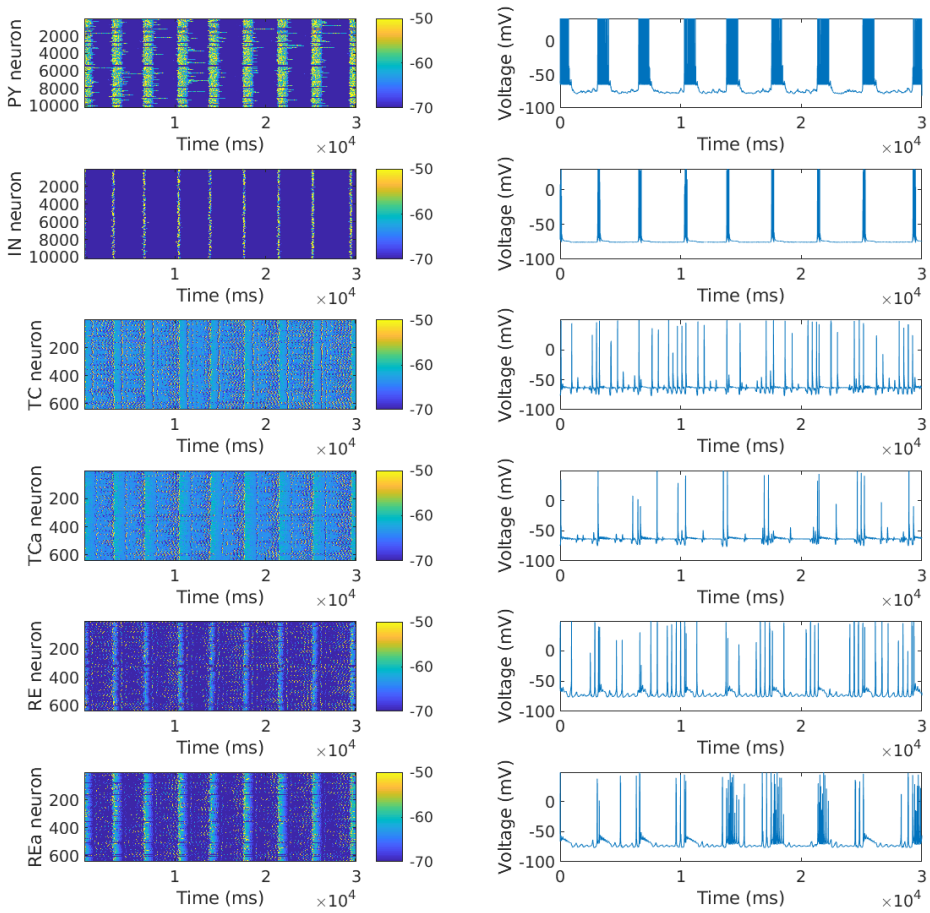

Figure S2. Activity of cortical inhibitory and thalamic RE and TC neurons in baseline model.

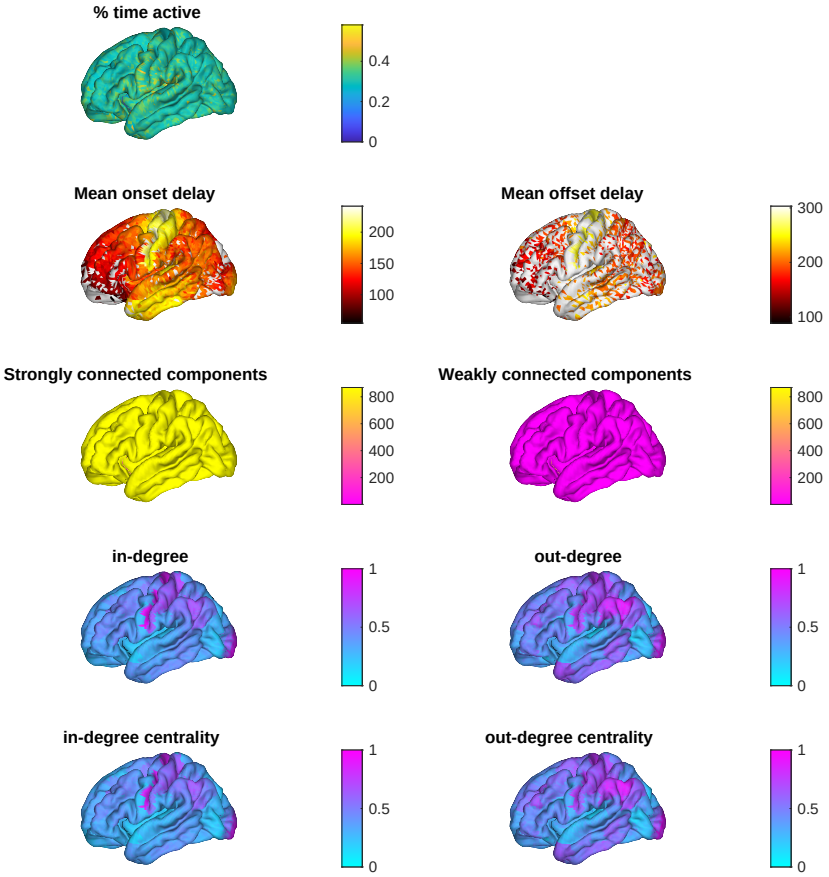

Figure S3. Graph properties for baseline network

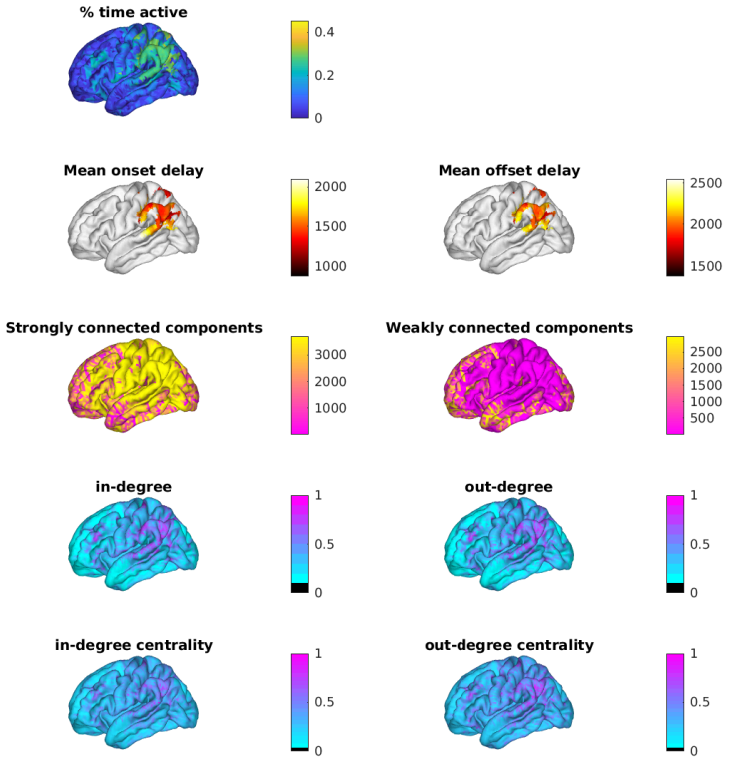

Figure S4. Graph properties for $R = 2.5$mm network

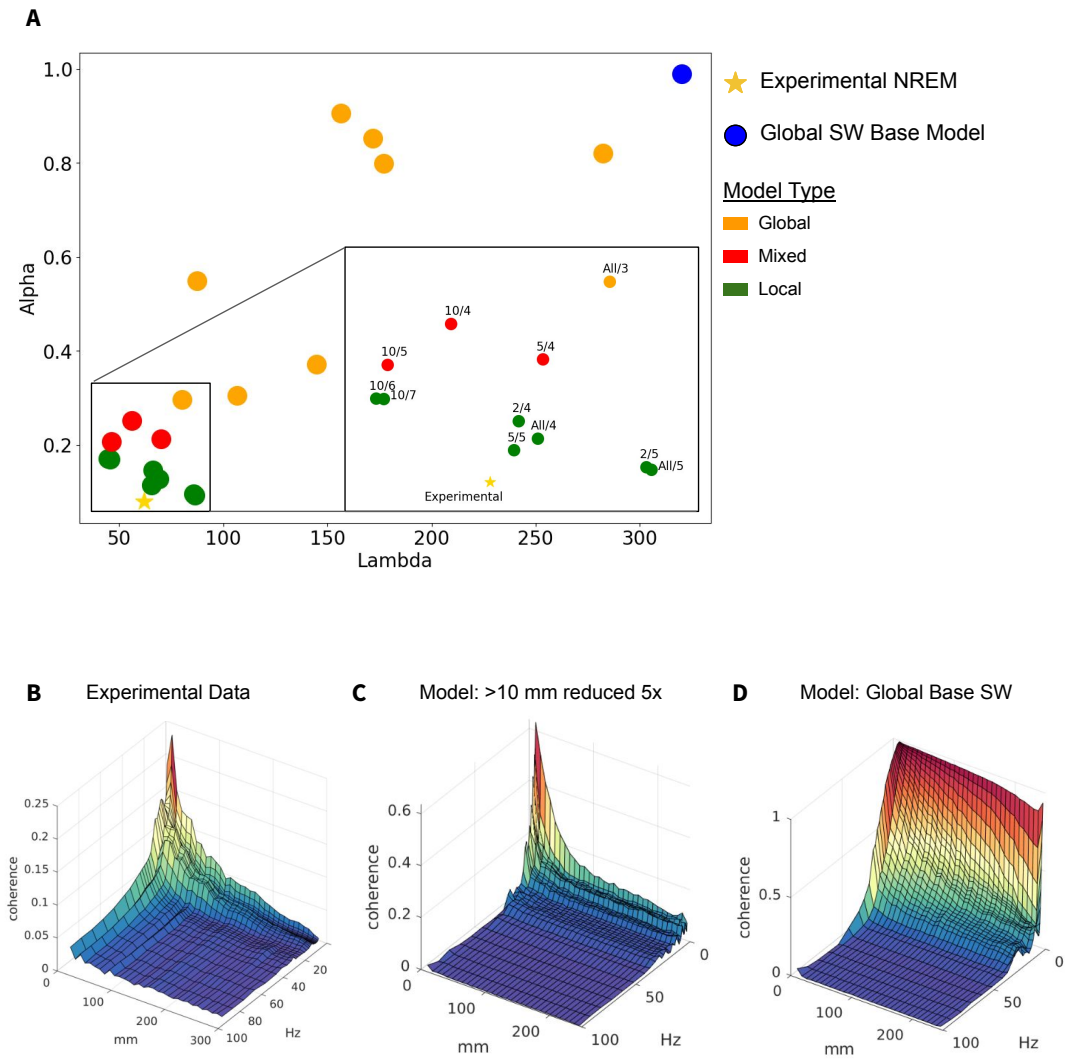

Figure S5. Scatter plot of coherence parameters per model with no added noise.